

AD-A097 592

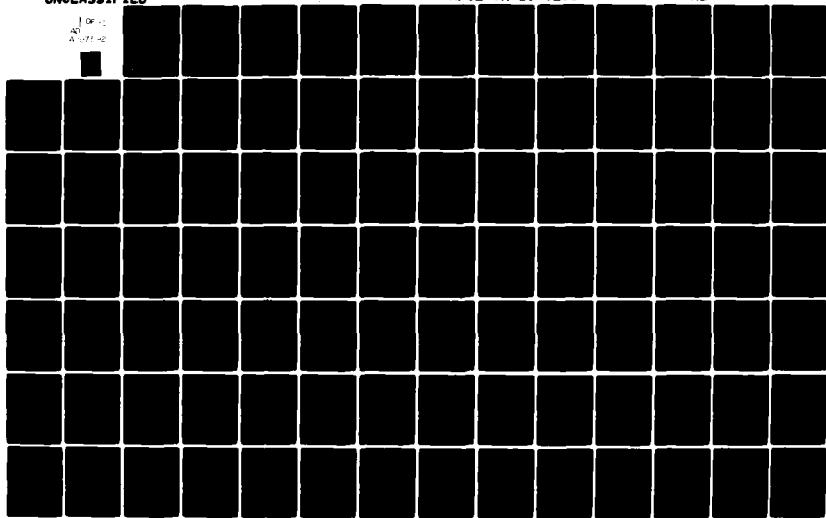
UTAH UNIV SALT LAKE CITY DEPT OF METEOROLOGY F/G 4/2
DEVELOPMENT OF INFRARED AND MICROWAVE TECHNIQUES FOR CLOUD PARA--ETC(U)
AUG 80 K LIOU, H Y YEH, F M CHEN, K HUTCHISON F19628-78-C-0130

UNCLASSIFIED

AFGL-TR-80-0263

NL

1 OF 1
AD
A097 592



AFGL-TR-80-0263

LEVEL #12

DEVELOPMENT OF INFRARED AND MICROWAVE TECHNIQUES
FOR CLOUD PARAMETER INFERENCE FROM SATELLITE
IMAGERY AND SOUNDER DATA

by

Kuo-Nan Liou, H. Y. Yeh, F. M. Chen, K. Hutchison
and E. Astling

Department of Meteorology
University of Utah
Salt Lake City, Utah 84112

30 August 1980

Final Report for Period
16 April 1978 to 30 July 1980

DTIC
SELECTED
APR 10 1981
A

Approved for public release; distribution unlimited

AIR FORCE GEOPHYSICS LABORATORY
AIR FORCE SYSTEM COMMAND
UNITED STATES AIR FORCE
HANSCOM AFB, MASSACHUSETTS 01731

AD A 097592

DTIC FILE COPY

81 4 10 011

Qualified requestors may obtain additional copies from the Defense Technical Information Center. All others should apply to the National Technical Information Service.

UNCLASSIFIED

SECURITY CLASSIFICATION OF THIS PAGE (When Data Entered)

19 REPORT DOCUMENTATION PAGE		READ INSTRUCTIONS BEFORE COMPLETING FORM
1. REPORT NUMBER 18 AFGL-TR-80-0263	2. GOVT ACCESSION NO. AD A097592	3. RECIPIENT'S CATALOG NUMBER 1
6. TITLE (and Subtitle) DEVELOPMENT OF INFRARED AND MICROWAVE TECHNIQUES FOR CLOUD PARAMETER INFERENCE FROM SATELLITE IMAGERY AND SOUNDER DATA.	5. STATE OF REPORT & PERIOD COVERED Final Report 16 Apr 1978-30 Jul 1980	
	6. PERFORMING ORG. REPORT NUMBER	
7. AUTHOR(s) Liou, H.Y., Yeh, F.M. Chen, K. Hutchison, E. Astling	15	8. CONTRACT OR GRANT NUMBER(s) F19628-78-C-0130
9. PERFORMING ORGANIZATION NAME AND ADDRESS Department of Meteorology University of Utah Salt Lake City, Utah 84112	16	10. PROGRAM ELEMENT, PROJECT, TASK AREA & WORK UNIT NUMBERS 62101F 667008AC 17/08
11. CONTROLLING OFFICE NAME AND ADDRESS Air Force Geophysics Laboratory Hanscom AFB, Massachusetts 01731 Contract Monitor: James T. Bunting/IYU	11	12. REPORT DATE 30 Aug 1980
		13. NUMBER OF PAGES 95
14. MONITORING AGENCY NAME & ADDRESS (if different from Controlling Office) 12 1<	15. SECURITY CLASS. (of this report) Unclassified	
	15a. DECLASSIFICATION DOWNGRADING SCHEDULE	
16. DISTRIBUTION STATEMENT (of this Report) Approved for public release; distribution unlimited.		
17. DISTRIBUTION STATEMENT (of the abstract entered in Block 20, if different from Report)		
18. SUPPLEMENTARY NOTES		
19. KEY WORDS (Continue on reverse side if necessary and identify by block number) Remote Sensing Satellite Meteorology Microwave Radiative Transfer Clouds and Precipitation ESMR Radiative Parameterization Nimbus VI Satellite SCAMS Weather Sensing HIRS		
20. ABSTRACT (Continue on reverse side if necessary and identify by block number) This report presents research to improve estimates of cloud parameters when both microwave and infrared data are available from weather satellites. The Defense Meteorological Satellite Program (DMSP) will have both types of data in 1983 with the first flight of the SSM/I multispectral microwave imager and improved cloud estimates could then be available to the AFGWC automated cloud analysis known as 3DNEPH. In this report, radiative transfer programs have been improved so that microwave channels can be		

DD FORM 1 JAN 73 1473

401103 24
SECURITY CLASSIFICATION OF THIS PAGE (When Data Entered)

simulated in a realistic manner. Also, the results of simulations have been compared to measurements from the ESMR, SCAMS, and HIRS sensors on the Nimbus VI satellite, which was the most complete set of microwave and infrared data available at the time of this study. The first area is concerned with the investigation of the effect of clouds and precipitation on the Nimbus VI ESMR channel and the use of ESMR vertical and horizontal polarization components for the determination of the liquid water content and cloud thickness. In conjunction with these objectives, we have developed a microwave radiative transfer program taking into account the polarization effect. Utilizing the microwave radiative transfer program, comparisons between the computed and observed brightness temperatures using the available radiosonde and surface observations are first carried out and theoretical sensitivity analyses then follow. A simple empirical-theoretical approach is subsequently taken to retrieve the cloud liquid water content and thickness. The second area deals with the use of both infrared and microwave channels for the cloud parameter inference parameterizations. The infrared and microwave radiative transfer programs are successively developed for retrieval of the high and low cloud top heights and thicknesses and the cloud liquid water content from selected HIRS and SCAMS channels of the Nimbus VI satellite. Random error analyses revealed that the cloud sounding technique employing a combination of infrared and microwave frequencies appears to be theoretically rigorous and practically workable. Thus, applications of the cloud sounding technique to the Nimbus VI HIRS and SCAMS data are carried out in which we have selected a number of cases associated with summertime convective cloud systems and wintertime large scale synoptic cyclones described in a previous report. The report presented detailed discussions on the surface and upper air observations, radar echoes, precipitation and other relevant synoptic features which were utilized to cross-check with the retrieved cloud parameters

Distribution	
Available	
Dist	Special

TABLE OF CONTENTS

	<u>Page</u>
ABSTRACT	
Section 1 INTRODUCTORY REMARKS	1
Section 2 INVESTIGATION OF CLOUD AND PRECIPITATION EFFECTS ON THE NIMBUS VI ESMR CHANNEL	4
2.1 Characteristics of the ESMR Channel	4
2.2 Microwave Radiative Transfer Including Polarization	6
2.2.1 Basic equations	6
2.2.2 General solution	9
2.2.3 Particular solution	13
2.2.4 Complete solution	15
2.2.5 Boundary condition	17
2.2.6 Solution matrix	18
2.2.7 Problem of surface emissivity	22
2.2.8 Problems associated with the eigenvalue	23
2.3 Comparisons between Calculated and Observed ESMR Brightness Temperatures for Selected Cases	25
2.4 Computational Results	29
2.4.1 Atmospheric profiles and cloud models	29
2.4.2 Unpolarized surface (over land)	31
2.4.3 Polarized surface (over calm water)	37
2.5 Liquid Water Content and Cloud Thickness Determination from ESMR 37 GHz Channel	47

	<u>Page</u>
Section 3 EXPLORATION OF CLOUD PARAMETER INFERENCE FROM A COMBINATION OF INFRARED AND MICROWAVE CHANNELS	53
3.1 Parameterization of Infrared Radiative Transfer for a Two-Layered Cloud System	53
3.2 High and Low Cloud Top and Thickness Determination from HIRS Channels	58
3.2.1 Determination of cirrus cloud top height	58
3.2.2 Determination of cirrus cloud thickness	62
3.2.3 Determination of low cloud top height	65
3.3 Parameterization of Microwave Radiative Transfer	67
3.4 Determination of Surface Emissivity and Liquid Water Content from SCAMS Channels	70
3.5 Results of Theoretical Analyses	75
3.6 Applications to Nimbus VI HIRS and SCAMS Data	78
Section 4 CONCLUSIONS	86
REFERENCES	90

SECTION 1

INTRODUCTORY REMARKS

In our previous research work concerning the development of cloud sounding techniques from orbiting meteorological satellites (Feddes and Liou, 1978; Liou and Duff, 1979), it was pointed out that a proper combination of infrared and microwave measurements could result in a significant improvement for the vertical and horizontal mapping of the cloud compositions and structure. In an effort to follow-up this idea and to provide a theoretically rigorous foundation for cloud sounding from satellites based on the theory of radiative transfer in scattering and absorbing atmospheres, we have proposed a program to integrate radiative transfer, remote sensing, and synoptic meteorology to further advance the development of cloud sounding techniques. The specific objectives of the present research project under the sponsorship of the Air Force Geophysics Laboratory have been (a) to develop a radiation model including polarization for microwave imagery channels, (b) to develop techniques for parameterizing the satellite microwave and infrared imagery and sounder data for the inference of cloud compositions and structure, and (c) to utilize the available ground truth data with varying degrees of visibility, thickness, and coverage for both cirriform and water clouds, including sources from weather station reports, radiosondes, radar summaries, and infrared pictures to cross check with the retrieved cloud parameters.

Within the scope of these objectives and subject to the time constraint and funding availability, we have utilized the comprehensive infrared and microwave data set from the Nimbus VI satellite and the

simultaneous synoptic reports, some of which are available through our previous research projects sponsored by the Air Force Geophysics Laboratory. In this report, we present two areas of research both of which are related to the determination of cloud parameters from meteorological satellites.

In Section 2 of this report, we investigate the effect of clouds and precipitation on the Nimbus VI ESMR channel and the use of ESMR vertical and horizontal components for the inference of the cloud thickness and the associated liquid water content over ocean surfaces. A microwave radiative transfer program, including polarization, has been developed and comparisons have been made between the computed and observed brightness temperatures utilizing the available radiosonde and surface observations. We then carry out the theoretical sensitivity analysis and develop a simple empirical-theoretical equation to retrieve the cloud thickness and liquid water content.

In Section 3 of this report, we develop and derive the necessary parameterization equations for infrared and microwave radiative transfer in conjunction with the inference of cloud parameters from satellites. The retrieval programs have been developed for the determination of the high cloud top height, high cloud thickness, low cloud top height, and cloud liquid water content successively utilizing selected HIRS and SCAMS channels. Hypothetical error analyses have been performed, and it is found that the retrieval technique appears to be theoretically rigorous and practically feasible. We then apply the cloud sounding technique to the Nimbus VI HIRS and SCAMS data for a number of carefully selected cases associated with summertime convective cloud systems and wintertime large scale synoptic cyclones described in a previous report by Astling and Liou (1979) and a master's thesis (Hall, 1979). We show that the satellite

retrieved cloud parameters from a combination of selected infrared and microwave channels appear to be in qualitative agreement with the available synoptic, radiosonde, surface, and radar observations. Further applications of the cloud sounding technique developed in this study for the mapping of three-dimensional cloud parameters over the globe seem feasible.

SECTION 2

INVESTIGATION OF CLOUD AND PRECIPITATION EFFECTS ON THE NIMBUS 6 ESMR CHANNEL

2.1 Characteristics of the ESMR Channel

The Nimbus 6 Electronically Scanning Microwave Radiometer (ESMR) receives the thermal microwave radiation upwelling from the earth's surface and atmosphere in a 250 MHz band centered at 37 GHz (0.81 cm). The antenna beam is scanned electrically through 71 discrete positions on each sweep. Each sweep takes 5.3 seconds. The nominal resolution is 20 km crosstrack and 45 km downtrack. Brightness temperatures are measured at each scan position. The data are intended for the mapping of the cloud liquid water content, the distribution and variation of sea ice cover and snow cover, and the characteristics of land surfaces.

The Nimbus 6 ESMR measures both horizontal and vertical polarization components by using two separate radiometer channels. The antenna beam of the ESMR scans ahead of the spacecraft along a conical surface with a constant angle of 45° with respect to the antenna axis (Fig. 2.1). The beam scans in azimuth 35° about the forward direction in 71 steps. In azimuth, the angular resolution varies from 0.95° when the beam position is straight ahead to 1.17° at the 35° scan extremes. In elevation it varies from 1° at the straight forward position to 0.84° at the extremes of the scan. The data are calibrated using warm (instrument ambient) and cold (cosmic background) inputs to the

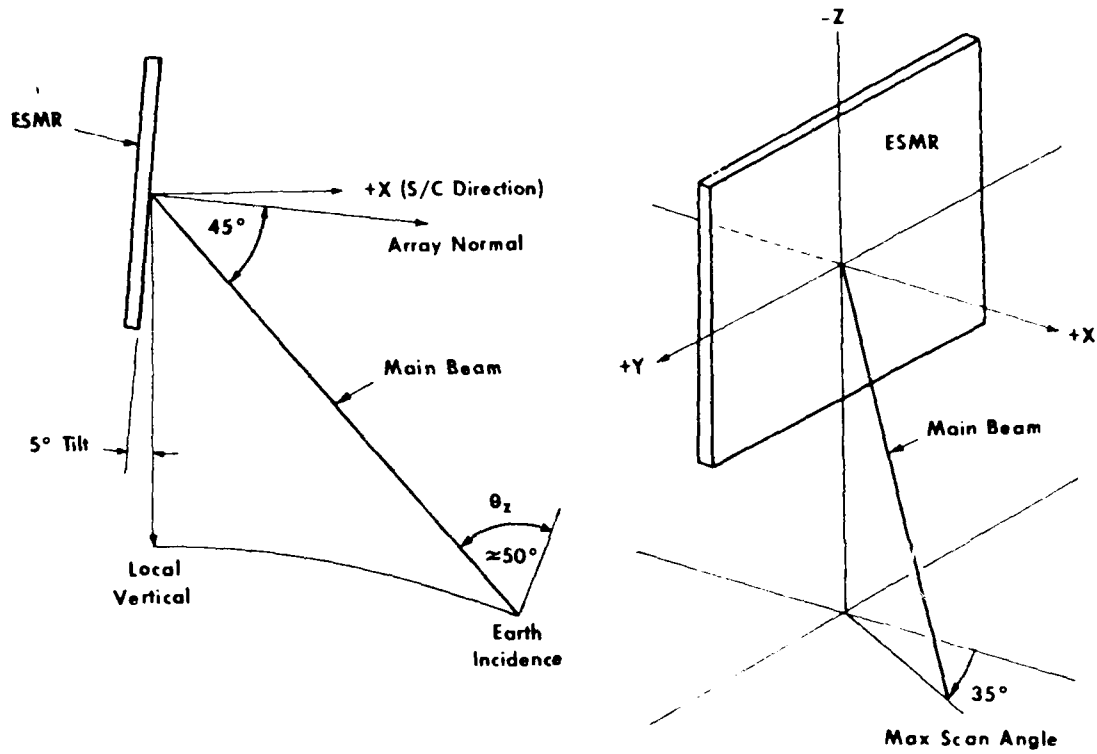


Fig. 2.1. ESMR antenna scan geometry.

radiometer. The weighting function for the 37 GHz channel with a surface emissivity of 0.9 is shown in Fig. 2.2. At this frequency, atmospheric absorption is mainly due to water vapor.

2.2 Microwave Radiative Transfer Including Polarization

2.2.1 Basic equations. Consider a plane-parallel cloud layer consisting of absorbing gases and particulates in local thermodynamic equilibrium and assume that thermal radiation from the earth atmosphere is independent of the azimuthal angle ϕ . We consider, separately, the radiance components I_p and I_r in the directions parallel and perpendicular, respectively, to the meridian plane containing the incident and emergent beams. The equations of radiative transfer governing the radiances I_p and I_r can be written in the form

$$\begin{aligned} \frac{dI_p(\nu, \tau; \mu)}{d\tau} &= I_p(\nu, \tau; \mu) - \omega_\nu [J_{p,p}(\nu, \tau; \mu) + J_{r,p}(\nu, \tau; \mu)] - (1 - \omega_\nu) B_\nu [T(\tau)], \\ \frac{dI_r(\nu, \tau; \mu)}{d\tau} &= I_r(\nu, \tau; \mu) - \omega_\nu [J_{p,r}(\nu, \tau; \mu) + J_{r,r}(\nu, \tau; \mu)] - (1 - \omega_\nu) B_\nu [T(\tau)], \end{aligned} \quad (2.1)$$

where μ is the cosine of the emergent angle θ which is with respect to the zenith, τ is the optical depth for cloud particles and gases within the cloud, T is the cloud temperature, and the single scattering albedo is

$$\omega_\nu = \frac{\rho S_{s,\nu}}{S_{s,\nu} + B_{a,\nu} + k_\nu \rho},$$

where $S_{s,\nu}$ and $B_{a,\nu}$ denote the volume scattering and absorption cross sections, respectively, for cloud particles at frequency ν , k_ν the gaseous absorption coefficient, ρ the gaseous density, B_ν denotes the

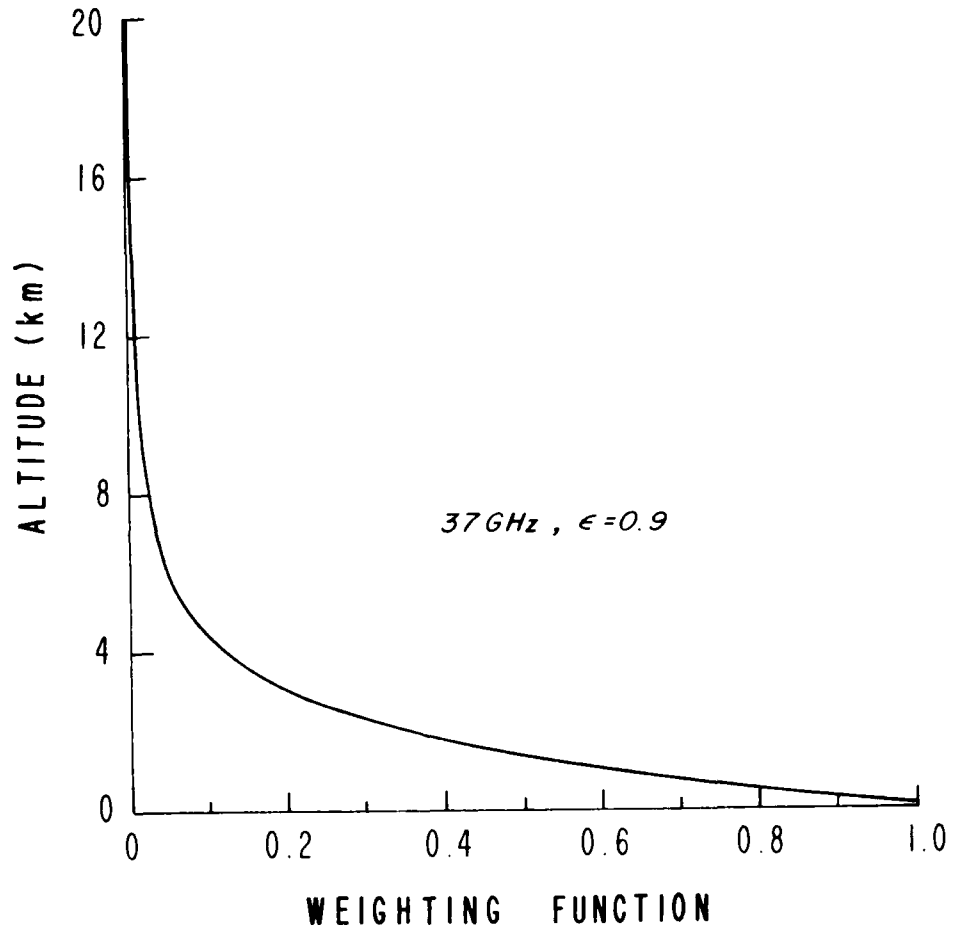


Fig. 2.2. Weighting function for the 37 GHz channel.

Planck function, and $J_{p',p}(\nu, \tau, \mu)$ is the scattering source term which transforms radiation polarized in the direction p' to the direction p . Chandrasekhar (1946) showed that if the phase matrix was determined by Rayleigh scattering, then the source terms are

$$\begin{aligned}
 J_{p',p}(\nu, \tau; \mu) &= \frac{3}{8} \int_{-1}^1 I_{p'}(\nu, \tau; \mu') [2(1-\mu'^2) + \mu^2(3\mu'^2 - 2)] d\mu' , \\
 J_{r,p}(\nu, \tau; \mu) &= \frac{3}{8} \mu^2 \int_{-1}^1 I_r(\nu, \tau; \mu') d\mu' , \\
 J_{v,r}(\nu, \tau; \mu) &= \frac{3}{8} \int_{-1}^1 I_v(\nu, \tau; \mu') \mu'^2 d\mu' , \\
 J_{r,r}(\nu, \tau; \mu) &= \frac{3}{8} \int_{-1}^1 I_r(\nu, \tau; \mu') d\mu' .
 \end{aligned} \tag{2.2}$$

Inserting Eq. (2.2) into Eq. (2.1), we find

$$\begin{aligned}
 \mu \frac{dI_{\ell}(\nu, \tau; \mu)}{d\tau} &= I_{\ell}(\nu, \tau; \mu) - \frac{3\tilde{\omega}_V}{8} \left\{ \int_{-1}^1 I_{\ell}(\nu, \tau; \mu') [2(1-\mu'^2) + \mu^2(3\mu'^2 - 2)] d\mu' \right. \\
 &\quad \left. + \mu^2 \int_{-1}^1 I_r(\nu, \tau; \mu') d\mu' \right\} - (1-\tilde{\omega}_V) B_V[T(\tau)] , \\
 \mu \frac{dI_r(\nu, \tau; \mu)}{d\tau} &= I_r(\nu, \tau; \mu) - \frac{3\tilde{\omega}_V}{8} \left[\int_{-1}^1 I_{\ell}(\nu, \tau; \mu') \mu'^2 d\mu' + \int_{-1}^1 I_r(\nu, \tau; \mu') d\mu' \right] \\
 &\quad - (1-\tilde{\omega}_V) B_V[T(\tau)] .
 \end{aligned} \tag{2.3}$$

The solutions of Eq. (2.3) and the numerical techniques for obtaining the spatial distribution of radiant intensity as a function of optical depth by using a discrete-ordinate method will be comprehensively

described in this section. For simplicity, we let $I_{\ell}(\nu, \tau; \mu_i) = I_{\ell i}$ and $I_r(\nu, \tau; \mu_i) = I_{ri}$. Upon replacing the integrals by the appropriate Gauss's quadrature in the n^{th} order approximation, we obtain the following systems of $4n$ linear equations in the forms

$$\begin{aligned} \mu_i \frac{dI_{\ell i}}{d\tau} &= I_{\ell i} - \frac{3\tilde{\omega}_\nu}{8} \left\{ 2 \sum_j a_j (1 - \mu_j^2) I_{\ell j} + \mu_i^2 \left[\sum_j a_j (3\mu_j^2 - 2) I_{\ell j} \right. \right. \\ &\quad \left. \left. + \sum_j a_j I_{rj} \right] \right\} - (1 - \tilde{\omega}_\nu) B_\nu [T(\tau)] , \\ \mu_i \frac{dI_{ri}}{d\tau} &= I_{ri} - \frac{3\tilde{\omega}_\nu}{8} \left(\sum_j a_j I_{rj} + \sum_j a_j \mu_j^2 I_{\ell j} \right) - (1 - \tilde{\omega}_\nu) B_\nu [T(\tau)] , \end{aligned} \quad (2.4)$$

where the index i and j are from $-n$ to n ($n \neq 0$), a_j represent the quadrature weights, and μ_j denotes the emergent angle at the discrete stream i . The complete solutions for the above differential equations assuming an isothermal cloud layer may be obtained by seeking a general solution for the homogeneous part plus adding a particular solution.

2.2.2 General solution. The homogeneous part of Eq. (2.4) may be written as

$$\begin{aligned} \mu_i \frac{dI_{\ell i}}{d\tau} &= I_{\ell i} - \frac{3\tilde{\omega}_\nu}{8} \left\{ 2 \sum_j a_j (1 - \mu_j^2) I_{\ell j} + \mu_i^2 \left[\sum_j a_j (3\mu_j^2 - 2) I_{\ell j} + \sum_j a_j I_{rj} \right] \right\} , \\ \mu_i \frac{dI_{ri}}{d\tau} &= I_{ri} - \frac{3\tilde{\omega}_\nu}{8} \left(\sum_j a_j I_{rj} + \sum_j a_j \mu_j^2 I_{\ell j} \right) . \end{aligned} \quad (2.5)$$

In order to obtain general solutions for Eq. (2.4), we let

$$I_{xi} = g_i e^{-k\tau}, \quad I_{ri} = h_i e^{-k\tau}, \quad i = 1, 2, \dots, n, \quad (2.6)$$

where g_i 's, h_i 's and k are certain constants. Substituting the expressions for I_{xi} and I_{ri} into Eq. (2.5), we obtain

$$\begin{aligned} (1+\mu_i k)g_i &= \frac{3\tilde{\omega}_v}{8} \{2\sum a_j(1-\mu_j^2)g_j + \mu_i^2[\sum a_j(3\mu_j^2-2)g_j + \sum a_j h_j]\}, \\ (1+\mu_i k)h_i &= \frac{3\tilde{\omega}_v}{8} (\sum a_j \mu_j^2 g_j + \sum a_j h_j). \end{aligned} \quad (2.7)$$

Eq. (2.7) implies that g_i and h_i may be expressed in the forms

$$g_i = \frac{\alpha \mu_i^2 + \beta}{1 + \mu_i k}, \quad h_i = \frac{\gamma}{1 + \mu_i k}, \quad i = 1, 2, \dots, n, \quad (2.8)$$

where α , β , and γ are certain constants, independent of i . Inserting Eq. (2.8) into Eq. (2.7) we have

$$\begin{aligned} \frac{\alpha \mu_i^2 + \beta}{1 + \mu_i k} (1 + \mu_i k) &= \frac{3\tilde{\omega}_v}{8} \{2\sum a_j(1-\mu_j^2) \frac{\alpha \mu_j^2 + \beta}{1 + \mu_j k} \\ &\quad + \mu_i^2[\sum a_j(3\mu_j^2-2) \frac{\alpha \mu_j^2 + \beta}{1 + \mu_j k} + \sum a_j \frac{\gamma}{1 + \mu_j k}]\}, \\ \frac{\gamma}{1 + \mu_i k} (1 + \mu_i k) &= \frac{3\tilde{\omega}_v}{8} (\sum a_j \mu_j^2 \frac{\alpha \mu_j^2 + \beta}{1 + \mu_j k} + \sum a_j \frac{\gamma}{1 + \mu_j k}). \end{aligned} \quad (2.9)$$

if we define the formula

$$D_m = \frac{3\tilde{\omega}_v}{8} \sum \frac{a_j \mu_j^m}{1 + \mu_j k}, \quad (2.10)$$

then Eq. (2.9) becomes

$$\alpha \mu_i^2 + \beta = \frac{3}{8} \{ 2[\alpha(D_2 - D_4) + \beta(D_0 - D_2)] + \mu_i^2 [\alpha(3D_4 - 2D_2) + \beta(3D_2 - 2D_0) + \gamma D_0] \},$$

$$\gamma = \frac{3}{8} (\alpha D_4 + \beta D_2 + \gamma D_0). \quad (2.11)$$

Since Eq. (2.10) is valid for all i , we must have

$$\frac{8}{3}\alpha = \alpha(3D_4 - 2D_2) + \beta(3D_2 - 2D_0) + \gamma D_0, \quad (2.12)$$

$$\frac{4}{3}\beta = \alpha(D_2 - D_4) + \beta(D_0 - D_2), \quad (2.13)$$

$$\frac{8}{3}\gamma = \alpha D_4 + \beta D_2 + \gamma D_0. \quad (2.14)$$

Eqs. (2.12) - (2.14) represent a system of homogeneous linear equations for α , β , and γ . In order to have non-trivial solutions the determinant of this system must vanish. Hence

$$\begin{vmatrix} 3D_4 - 2D_2 - \frac{8}{3} & 3D_2 - 2D_0 & D_0 \\ D_2 - D_4 & D_0 - D_2 - \frac{4}{3} & 0 \\ D_4 & D_2 & D_0 - \frac{8}{3} \end{vmatrix} = 0. \quad (2.15)$$

By adding or subtracting suitable multiples of the rows or columns we

can transform the determinant on the left-hand side successively into

$$\begin{aligned}
 & \begin{vmatrix} 3D_4 - 2D_2 - \frac{8}{3} & 3D_2 - 2D_0 & D_0 \\ D_2 & D_0 - \frac{4}{3} & D_0 - \frac{8}{3} \\ D_4 & D_2 & D_0 - \frac{8}{3} \end{vmatrix} \\
 = & \begin{vmatrix} -\frac{8}{3} & -\frac{8}{3} & \frac{8}{3} \\ D_2 & D_0 - \frac{4}{3} & D_0 - \frac{8}{3} \\ D_4 & D_2 & D_0 - \frac{8}{3} \end{vmatrix} \\
 = & \begin{vmatrix} 0 & 0 & \frac{8}{3} \\ D_2 + D_0 - \frac{8}{3} & 2(D_0 - 2) & D_0 - \frac{8}{3} \\ D_4 + D_0 - \frac{8}{3} & D_2 + D_0 - \frac{8}{3} & D_0 - \frac{8}{3} \end{vmatrix} \quad (2.16)
 \end{aligned}$$

Hence

$$(D_0 + D_2 - \frac{8}{3})^2 - 2(D_4 + D_0 - \frac{8}{3})(D_0 - 2) = 0. \quad (2.17)$$

Eq. (2.17) is of order $4n$ in k and admits, in general, $4n$ distinct non-vanishing roots which must occur in pairs and

$$k_{+\alpha} = -k_{-\alpha}, \quad \alpha = 1, 2, \dots, 2n. \quad (2.18)$$

From the relations in Eqs. (2.12) - (2.14) we can express β and γ in terms of D_0 , D_2 , D_4 , and α to get

$$\beta = \frac{-(D_2 - D_4)}{D_0 - D_2 - \frac{4}{3}} \alpha,$$

$$\gamma = \frac{D_2^2 + \frac{4}{3}D_4 - D_0D_4}{(D_0 - D_2 - \frac{4}{3})(D_0 - \frac{8}{3})} \alpha. \quad (2.19)$$

Thus, from Eqs. (2.6), (2.8), and (2.19), we obtain

$$I_{li} = \text{const.} \frac{\mu_i^2 - (D_2 - D_4)/(D_0 - D_2 - \frac{4}{3})}{1 + \mu_i k_{i\alpha}} e^{-k_{i\alpha} \tau},$$

$$I_{ri} = \text{const.} \frac{D_2^2 + \frac{4}{3}D_4 - D_0D_4}{(1 + \mu_i k_{i\alpha})(D_0 - D_2 - \frac{4}{3})(D_0 - \frac{8}{3})} e^{-k_{i\alpha} \tau}, \quad (2.20)$$

$$i=1, 2, \dots, n, \quad \alpha=1, 2, \dots, 2n.$$

The general solution can now be written as

$$I_{li} = \sum_{\alpha=-2n}^{2n} M_{\alpha} \frac{\mu_i^2 - (D_2 - D_4)/(D_0 - D_2 - \frac{4}{3})}{1 + \mu_i k_{i\alpha}} e^{-k_{i\alpha} \tau},$$

$$I_{ri} = \sum_{\alpha=-2n}^{2n} M_{\alpha} \frac{D_2^2 + \frac{4}{3}D_4 - D_0D_4}{(1 + \mu_i k_{i\alpha})(D_0 - D_2 - \frac{4}{3})(D_0 - \frac{8}{3})} e^{-k_{i\alpha} \tau}, \quad (2.21)$$

where M_{α} ($\alpha=-2n, \dots, 2n$) are $4n$ constants of integration.

2.2.3 Particular solution. To complete the solutions for the system of equations denoted in Eq. (2.4), a particular solution is required.

It can be obtained by letting

$$I_{\ell i} = C_{\ell}, \quad I_{ri} = C_r. \quad (2.22)$$

Inserting Eq. (2.22) into Eq. (2.4) and performing integration we have

$$0 = C_{\ell} - \frac{3\tilde{\omega}_V}{8} \left(\frac{8}{3} C_{\ell} - 2\frac{2}{i} C_{\ell} + 2\frac{2}{i} C_r \right) - (1-\tilde{\omega}_V) B_V[T(\tau)],$$

$$0 = C_r - \frac{3\tilde{\omega}_V}{8} \left(\frac{2}{3} C_{\ell} + 2C_r \right) - (1-\tilde{\omega}_V) B_V[T(\tau)]. \quad (2.23)$$

Eq. (2.23) can be rewritten as

$$(1-\tilde{\omega}_V + \frac{3}{4} \frac{\tilde{\omega}_V}{i} \frac{2}{i}) C_{\ell} - \frac{3}{4} \frac{\tilde{\omega}_V}{i} \frac{2}{i} C_r = (1-\tilde{\omega}_V) B_V[T(\tau)],$$

$$- \frac{\tilde{\omega}_V}{4} C_{\ell} + (1 - \frac{3}{4} \frac{\tilde{\omega}_V}{i}) C_r = (1-\tilde{\omega}_V) B_V[T(\tau)]. \quad (2.24)$$

From Eq. (2.24) we note

$$(1 - \frac{3}{4} \frac{\tilde{\omega}_V}{i} + \frac{3}{4} \frac{\tilde{\omega}_V}{i} \frac{2}{i}) C_{\ell} - (\frac{3}{4} \frac{\tilde{\omega}_V}{i} \frac{2}{i} + 1 - \frac{3}{4} \frac{\tilde{\omega}_V}{i}) C_r = 0.$$

It follows that

$$C_{\ell} = C_r \quad (2.25)$$

Substitution of Eq. (2.25) into Eq. (2.24) leads to

$$(1-\tilde{\omega}_V) C_{\ell} = (1-\tilde{\omega}_V) B_V[T(\tau)].$$

Thus, the particular solution is simply

$$I_{l,i} = I_{r,i} = B_v[T(\tau)]. \quad (2.26)$$

2.2.4 Complete solution. Combining the solutions given by Eqs. (2.21) and (2.26), the complete solutions for Eq. (2.4) may be expressed in the form

$$I_{l,i} = \sum_{\alpha=-2n}^{2n} M_{\alpha} \psi_{\alpha}(\mu_i) e^{-k_{\alpha}\tau} + B_v[T(\tau)],$$

$$I_{r,i} = \sum_{\alpha=-2n}^{2n} M_{\alpha} \phi_{\alpha}(\mu_i) e^{-k_{\alpha}\tau} + B_v[T(\tau)], \quad (2.27)$$

where ψ_{α} , and ϕ_{α} represent the eigenfunctions, k_{α} the eigenvalues of the differential equations, and M_{α} a set of constants of proportionality to be determined from the radiation boundary conditions above and below the cloud layer.

In the frequency domain, the Planck function is given by

$$B_v[T(\tau)] = 2h\nu^3/[c^2(e^{h\nu/KT}-1)], \quad (2.28)$$

where h is the Planck constant, K the Boltzmann constant, and c the velocity of light. In the microwave region, the Rayleigh-Jeans approximation for the Planck function may be utilized and we find ($h\nu/KT \rightarrow 0$)

$$B_v(T) \approx (2\nu^2 K/c^2)T. \quad (2.29)$$

Eq. (2.29) states that the Planck radiance is linearly proportional to the temperature. Furthermore, radiometers which measure the thermal

emission are usually calibrated with sources at a certain reference temperature. Thus, we may define an equivalent brightness temperature T_B such that

$$I_{\nu} = (2\nu^2 k/c^2) T_B(\nu) \quad (2.30)$$

Using Eqs. (2.29) and (2.30), Eq. (2.3) may be written in terms of the brightness temperature as follows

$$\begin{aligned} \mu \frac{dT_{B\ell}(\nu, \tau; \mu)}{d\tau} = & T_{B\ell}(\nu, \tau; \mu) - \frac{3\tilde{\omega}_{\nu}}{8} \left[\int_{-1}^1 T_{B\ell}(\nu, \tau; \mu') [2(1-\mu'^2) \right. \\ & \left. + \mu'^2(3\mu'^2-2)] d\mu' + \mu^2 \int_{-1}^1 T_{Br}(\nu, \tau; \mu') d\mu' \right] - (1-\tilde{\omega}_{\nu})T(\tau), \end{aligned}$$

$$\begin{aligned} \mu \frac{dT_{Br}(\nu, \tau; \mu)}{d\tau} = & T_{Br}(\nu, \tau; \mu) - \frac{3\tilde{\omega}_{\nu}}{8} \left[\int_{-1}^1 T_{B\ell}(\nu, \tau; \mu') \mu'^2 d\mu' \right. \\ & \left. + \int_{-1}^1 T_{Br}(\nu, \tau; \mu') d\mu' \right] - (1-\tilde{\omega}_{\nu})T(\tau) . \end{aligned} \quad (2.31)$$

The solutions in terms of the temperature field can be derived in a manner similar to the procedures outlined previously and may be written in the form

$$\begin{aligned} T_{B\ell}(\nu, \tau; \mu_i) &= \sum_{\alpha=-2n}^{2n} M'_{\alpha} \psi_{\alpha}(\mu_i) e^{-k_{\alpha} \tau} + T_C , \\ T_{Br}(\nu, \tau; \mu_i) &= \sum_{\alpha=-2n}^{2n} M'_{\alpha} \phi_{\alpha}(\mu_i) e^{-k_{\alpha} \tau} + T_C , \end{aligned} \quad (2.32)$$

where we note that the constants of proportionality M'_{it} differ from those given in Eq. (2.26) and are to be evaluated from the radiation boundary conditions in terms of the temperature field. Note that T_c , the cloud temperature, is independent of frequency.

2.2.5 Boundary condition. In this study, it is assumed that the cloud layer is isothermal and homogeneous with respect to the cloud composition. At the cloud top, the downward brightness temperature is equal to the brightness contributions from every point in the atmosphere above the cloud top. Thus, we write

$$T_{Bp}(\nu, z_t; -\mu_i) = \int_{z=z_t}^{\infty} T(z) d\tau''_{\nu}(z, z_t; -\mu_i), \quad p=l, r, \quad (2.33)$$

where z_t is the height of the cloud top and $-\mu_i$ indicates that radiation transfer is downward. Here we change the τ -coordinates to the height coordinates for the convenience of discussion. The transmittance in this equation is given by

$$T_{\nu}(z_t, z; -\mu_i) = T'_{\nu}(z, z_t; -\mu_i) = \exp\left[-\frac{1}{\mu_i} \int_{z_t}^z k_{\nu}(z') \mu(z') dz'\right]. \quad (2.34)$$

It is convenient to express the transmittance in reference to the top of the atmosphere in the form

$$\begin{aligned} T_{\nu}(z_t, z; \mu_i) &= T_{\nu}(z_t, \infty; \mu_i) / T_{\nu}(z, \infty; \mu_i) \\ &= T_{\nu}(z_t, \mu_i) / T_{\nu}(z; \mu_i), \quad z_t > z. \end{aligned} \quad (2.35)$$

At the bottom of the cloud, two conditions are considered. The first

one is for a nonpolarizing surface (such as land) while the other is for polarizing surface (such as calm water).

For a nonpolarizing surface, the radiation incident on the cloud base consists of three components; (a) the surface contribution, (b) the direct atmospheric contribution from below the cloud, and (c) the reflected atmospheric contribution from below the cloud. The lower boundary condition can then be expressed as

$$T_{Bp}(v, z_b; +\mu_i) = \epsilon_v T_{Sv}''(0, z_b; +\mu_i) + \int_0^{z_b} T(z) dT_v(z, z_b; +\mu_i) \\ + (1 - \epsilon_v) T_v(0, z_b; +\mu_i) \int_0^{z_b} T(z) dT_v(0, z; -\mu_i), \quad p=\ell, r \quad (2.36)$$

where z_b is the height of the cloud base.

For a polarizing surface, we have

$$T_{Bp}(v, z_b; +\mu_i) = \epsilon_{vp}(\mu_i) T_{Sv}''(0, z_b; +\mu_i) + \int_0^{z_b} T(z) dT_v(z, z_b; +\mu_i) \\ + [1 - \epsilon_{vp}(\mu_i)] T_v(0, z_b; +\mu_i) \int_0^{z_b} T(z) dT_v(0, z; -\mu_i), \quad p=\ell, r \quad (2.37)$$

Each term on the right-hand side of Eq. (2.37) has the same meaning as that in Eq. (2.36). Note that the emissivity varies with the discrete stream employed and with parallel and vertical polarization components.

2.2.6 Solution matrix. Upon applying the boundary conditions, Eq. (2.32) becomes

$$\sum_{\alpha} M'_{\alpha} \psi_{\alpha}(-\mu_j) = T_{Bl}(v, z_t; -\mu_j) - T_c, \quad (2.38)$$

$$\sum_{\alpha} M'_{\alpha} \phi_{\alpha}(-\mu_j) = T_{Br}(v, z_t; -\mu_j) - T_c, \quad (2.39)$$

$$\sum_{\alpha} M'_{\alpha} \xi_{\alpha}(\mu_j) = T_{Bl}(v, z_b; \mu_j) - T_c, \quad (2.40)$$

$$\sum_{\alpha} M'_{\alpha} \eta_{\alpha}(\mu_j) = T_{Br}(v, z_b; \mu_j) - T_c, \quad (2.41)$$

where

$$\xi_{\alpha}(\mu_j) = \psi_{\alpha}(\mu_j) e^{-k_{\alpha} \tau^*}, \quad (2.42)$$

$$\eta_{\alpha}(\mu_j) = \phi_{\alpha}(\mu_j) e^{-k_{\alpha} \tau^*}, \quad (2.43)$$

and τ^* is the total optical thickness of the cloud.

Eqs. (2.38) - (2.41) represent a system of $4n$ linear equations from which the M coefficients may be determined by using standard matrix inversion techniques. In terms of matrix operation we may express

$$\vec{\Phi} \vec{M} = \vec{B}. \quad (2.44)$$

The coefficient matrix in Eq. (2.44) is

$$\hat{M} = \begin{pmatrix} M_{-2n} \\ M_{-2n+1} \\ \vdots \\ M_{-n} \\ \vdots \\ M_{-1} \\ M_1 \\ \vdots \\ M_n \\ \vdots \\ M_{2n-1} \\ M_{2n} \end{pmatrix} \quad (2.45)$$

The matrix denoting the contributions due to cloud emission and upward and downward radiances reaching the cloud base and top, respectively, may be written as

$$\hat{B} = \begin{pmatrix} T_{B\uparrow}(\nu, z_t; -\mu_n) - T_c \\ \vdots \\ T_{B\uparrow}(\nu, z_t; -\mu_1) - T_c \\ T_{B\downarrow}(\nu, z_t; -\mu_n) - T_c \\ \vdots \\ T_{B\downarrow}(\nu, z_t; -\mu_1) - T_c \\ T_{B\downarrow}(\nu, z_b; \mu_1) - T_c \\ \vdots \\ T_{B\downarrow}(\nu, z_b; \mu_n) - T_c \\ T_{B\uparrow}(\nu, z_b; \mu_1) - T_c \\ \vdots \\ T_{B\uparrow}(\nu, z_b; \mu_n) - T_c \end{pmatrix} \quad (2.46)$$

and finally, the $4n$ by $4n$ matrix

$$\vec{\phi} = \begin{bmatrix} \psi_{-2n}(-\mu_n) & \dots & \psi_{-1}(-\mu_n) & \psi_1(-\mu_n) & \dots & \psi_{2n}(-\mu_n) \\ \vdots & & \vdots & \vdots & & \vdots \\ \psi_{-2n}(-\mu_1) & \dots & \psi_{-1}(-\mu_1) & \psi_1(-\mu_1) & \dots & \psi_{2n}(-\mu_1) \\ \vdots & & \vdots & \vdots & & \vdots \\ \psi_{-2n}(-\mu_n) & \dots & \psi_{-1}(-\mu_n) & \psi_1(-\mu_n) & \dots & \psi_{2n}(-\mu_n) \\ \vdots & & \vdots & \vdots & & \vdots \\ \psi_{-2n}(-\mu_1) & \dots & \psi_{-1}(-\mu_1) & \psi_1(-\mu_1) & \dots & \psi_{2n}(-\mu_1) \\ \vdots & & \vdots & \vdots & & \vdots \\ \epsilon_{-2n}(\mu_1) & \dots & \epsilon_{-1}(\mu_1) & \epsilon_1(\mu_1) & \dots & \epsilon_{2n}(\mu_1) \\ \vdots & & \vdots & \vdots & & \vdots \\ \epsilon_{-2n}(\mu_n) & \dots & \epsilon_{-1}(\mu_n) & \epsilon_1(\mu_n) & \dots & \epsilon_{2n}(\mu_n) \\ \vdots & & \vdots & \vdots & & \vdots \\ \eta_{-2n}(\mu_1) & \dots & \eta_{-1}(\mu_1) & \eta_1(\mu_1) & \dots & \eta_{2n}(\mu_1) \\ \vdots & & \vdots & \vdots & & \vdots \\ \eta_{-2n}(\mu_n) & \dots & \eta_{-1}(\mu_n) & \eta_1(\mu_n) & \dots & \eta_{2n}(\mu_n) \end{bmatrix} \quad (2.47)$$

Having the above information, we may now carry out the computations for the evaluation of M'_α 's simultaneously by means of a matrix inversion method. Consequently, values of M'_α 's may be inserted into Eq. (2.32) to obtain the brightness temperature distribution.

The microwave transfer program for cloud layers will give the upward brightness temperature at the cloud top, i.e., $T_B(\nu, z_t; \mu_i)$. Thus, the upward brightness temperature at the satellite point in overcast cloudy conditions may then be written as

$$T_B(\nu, \infty; \mu_i) = T_B(\nu, z_t; \mu_i) T_\nu(z_t, \infty; \mu_i) + \int_{z_t}^{\infty} T(z) dT_\nu(z, \infty; \mu_i), \quad (2.48)$$

where the first term in the right-hand side of Eq. (2.48) represents

the contribution from the cloud top brightness which is being attenuated to the top of the atmosphere, and the remaining term is the atmospheric contribution above the cloud top. For applications to the 37 GHz ESMR channel, computations are carried out for the emergent angle of 50°.

2.2.7 Problem of surface emissivity. A special problem area in the use of microwave for atmospheric sounding from a satellite platform is the surface emissivity in the microwave spectrum, emissivity values of the earth's surface vary over a considerable range, from about 0.4 to 1. Emissivity of the water surface depends upon such variables as salinity, temperature, and frequency. The brightness temperature of a calm sea depends on the salinity and temperature of the water, the frequency, polarization, and incidence angle. Over land, on the other hand, the emissivity depends on the moisture content of the soil. Wetting of a soil surface results in a rapid decrease in the emissivity value. The surface emissivity appearing in the first term on the righthand side of Eq. (2.36) has a significant effect on the brightness temperature value.

By assuming an electromagnetically smooth surface, the emissivity can be expressed by

$$\epsilon_v = 1 - r_v^2, \quad (2.49)$$

where the Fresnel reflection coefficient for the air-water interface is given by

$$|r_{v,h}|^2 = \frac{(\cos\theta_i - p)^2 + q^2}{(\cos\theta_i + p)^2 + q^2},$$

$$|r_{v,v}|^2 = \frac{[(m_r^2 - m_i^2)\cos\theta_i - p]^2 + (2m_r m_i \cos\theta_i - q)^2}{[(m_r^2 - m_i^2)\cos\theta_i + p]^2 + (2m_r m_i \cos\theta_i + q)^2}. \quad (2.50)$$

The subscripts v and h refer to the vertically and horizontally polarized components, respectively. The angle of incidence is denoted as θ_i and the variables p and q are given by

$$p^2 = \frac{1}{2} \{m_r^2 - m_i^2 - \sin^2\theta_i + [(m_r^2 - m_i^2 - \sin^2\theta_i)^2 + 4m_r^2 m_i^2]^{1/2}\},$$

$$q^2 = \frac{1}{2} \{-(m_r^2 - m_i^2 - \sin^2\theta_i) + [(m_r^2 - m_i^2 - \sin^2\theta_i)^2 + 4m_r^2 m_i^2]^{1/2}\}, \quad (2.51)$$

where m_r and m_i are real and imaginary parts of the relative refractive index of water which is directly related to the dielectric properties of the surface.

2.2.8 Problems associated with the eigenvalue. Fig. 2.3 illustrates a typical distribution of eigenvalues for Rayleigh scattering with a single scattering albedo of 0.4128. On the basis of the characteristic equation denoted in Eq. (2.17) and the definition of D's in Eq. (2.10), it can be easily found that as $k_i \rightarrow \mu_1^{-1}$, $f(k_i) \rightarrow -\infty$. In this figure, the same intervals between each μ_i^{-1} are plotted so that lines across the zeros could be clearly presented. It is evident that each interval contains two eigenvalues. Although the numerical scheme for the solution

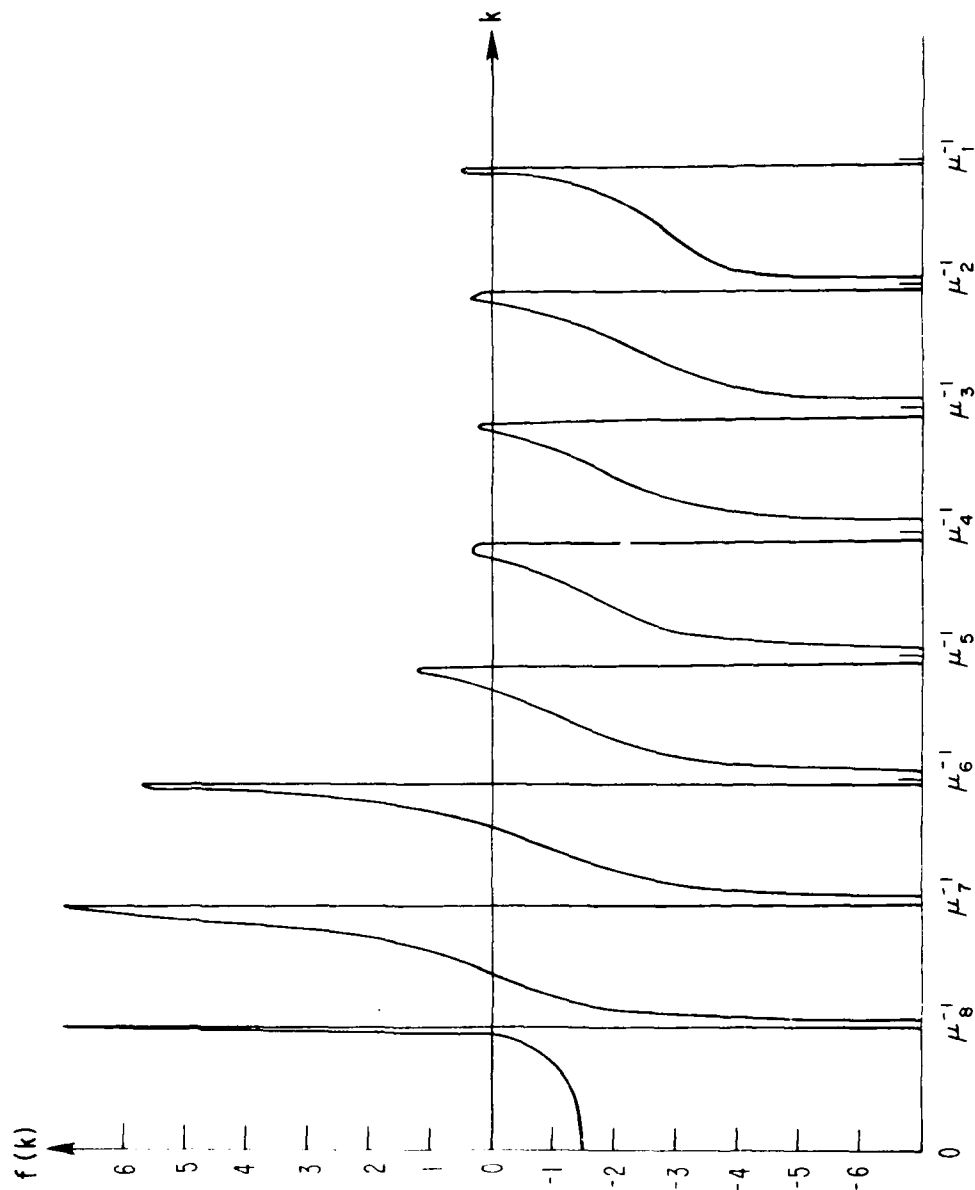


Fig. 2.3. A typical distribution of eigenvalues for Rayleigh scattering.

of Eq. (2.17) is straightforward, we find in the numerical computations that unstable results for the intensity distribution are frequently generated due to small eigenvalues. Thus, extensive experiments utilizing Eq. (2.17) for seeking the eigenvalues corresponding to different single scattering albedos have been carried out to obtain stable computations under various atmospheric conditions. It is found that with the accuracy of the eigenvalues k_i up to eight decimal points, the intensities obtained from the theoretical radiative transfer program for the cases with a rainfall rate less than 10 mm/hr are all stable. Here the meaning of "stable" is used such that an increase in the accuracy of k_i to about four decimal points does not affect the intensity results.

2.3 Comparisons Between Calculated and Observed ESMR Brightness Temperatures for Selected Cases

In this section we report the results of comparisons between calculated and observed brightness temperatures for the ESMR channel. The basic criterion for the selection of the ESMR 37 GHz data for comparison with the computed values is that the surface report and radiosonde data must be available under the satellite pass. Additionally, a variety of atmospheric conditions and surface characteristics are chosen so that comparisons are not limited to specific cases. In the theoretical calculations, a 50° zenith angle was used in order to match the observed data from the ESMR channels. 19 cases were selected at or near the Nimbus 6 satellite subtrack on August 25, 1975 and February 20 and 21, 1976. The points were selected when the radiosonde data and the surface weather report were available within 30 km, and the time of the

satellite pass was within six hours before or after the time of local sounding.

The Nimbus 6 has an equator crossing time of approximately 1800 Z for the United States passes. Thus, the surface report and radiosonde data for either 1200 Z or 0000 Z were used. We have collected 11 clear cases, four nonprecipitating cloudy cases, and four precipitating cloudy cases. Among the 11 clear cases, five were considered to be over polarized surfaces since these stations were quite close to the ocean surface over which the observed ESMR data showed strong polarization.

In order to have a reasonable comparison between the computed and observed brightness temperatures, the surface emissivity must be obtained objectively. In this study, we utilize the scheme proposed by Waters et al. (1975) described in Section 3.4 to determine the surface emissivity which involves the use of SCAMS channels 1 (22.235 GHz) and 2 (31.4 GHz). Since the water vapor transmittance and the refractive index of water at 37 GHz are very close to those at 31.4 GHz, we have assumed that the surface reflectivity derived for 31.4 GHz also is valid for 37 GHz. Consequently, using the observed ESMR data, surface emissivities for both polarization components may be estimated.

In Figs. 2.4 and 2.5, the computed brightness temperatures for both horizontal and vertical polarization components are compared with the Nimbus 6 ESMR data. Generally, fairly good agreement can be seen between the computed results and observed data. For those over polarized surfaces, the computed results obtained from the radiative transfer

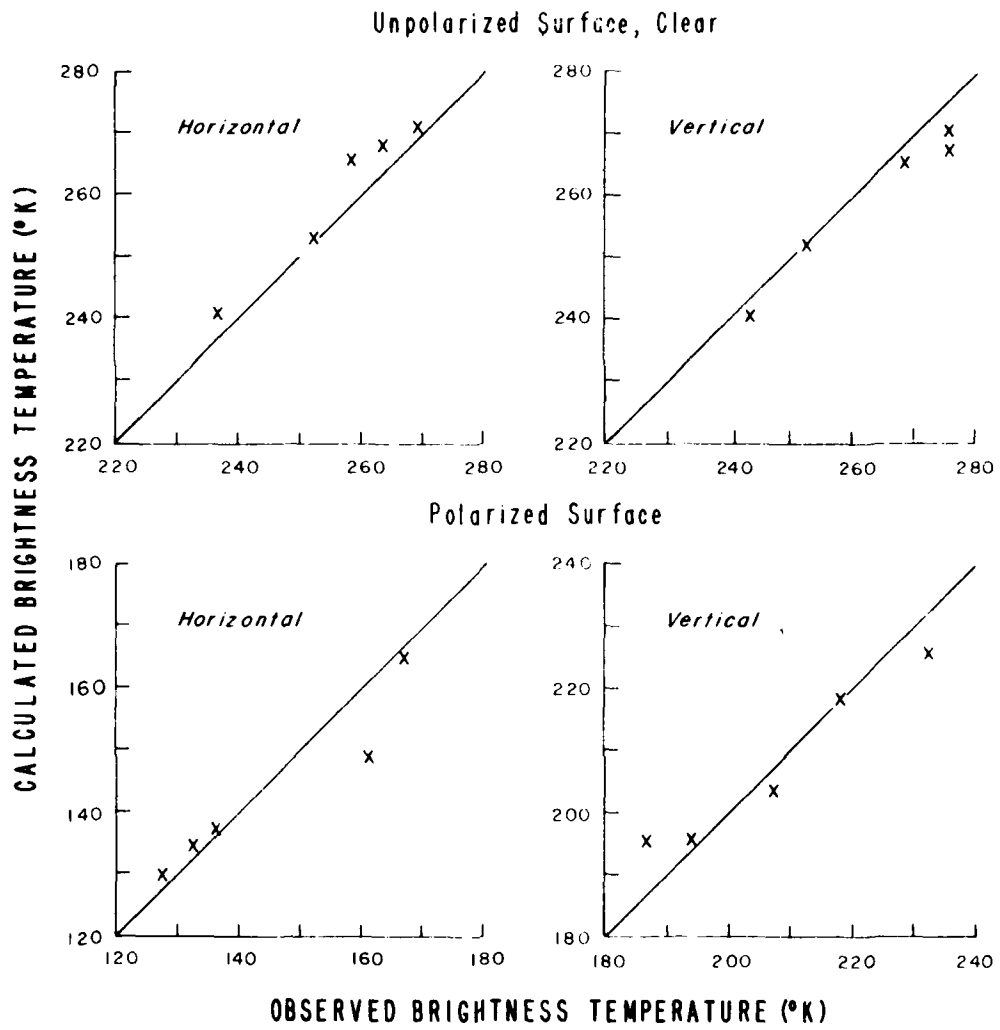


Fig. 2.4. Comparisons between calculated and observed brightness temperatures for selected clear cases.

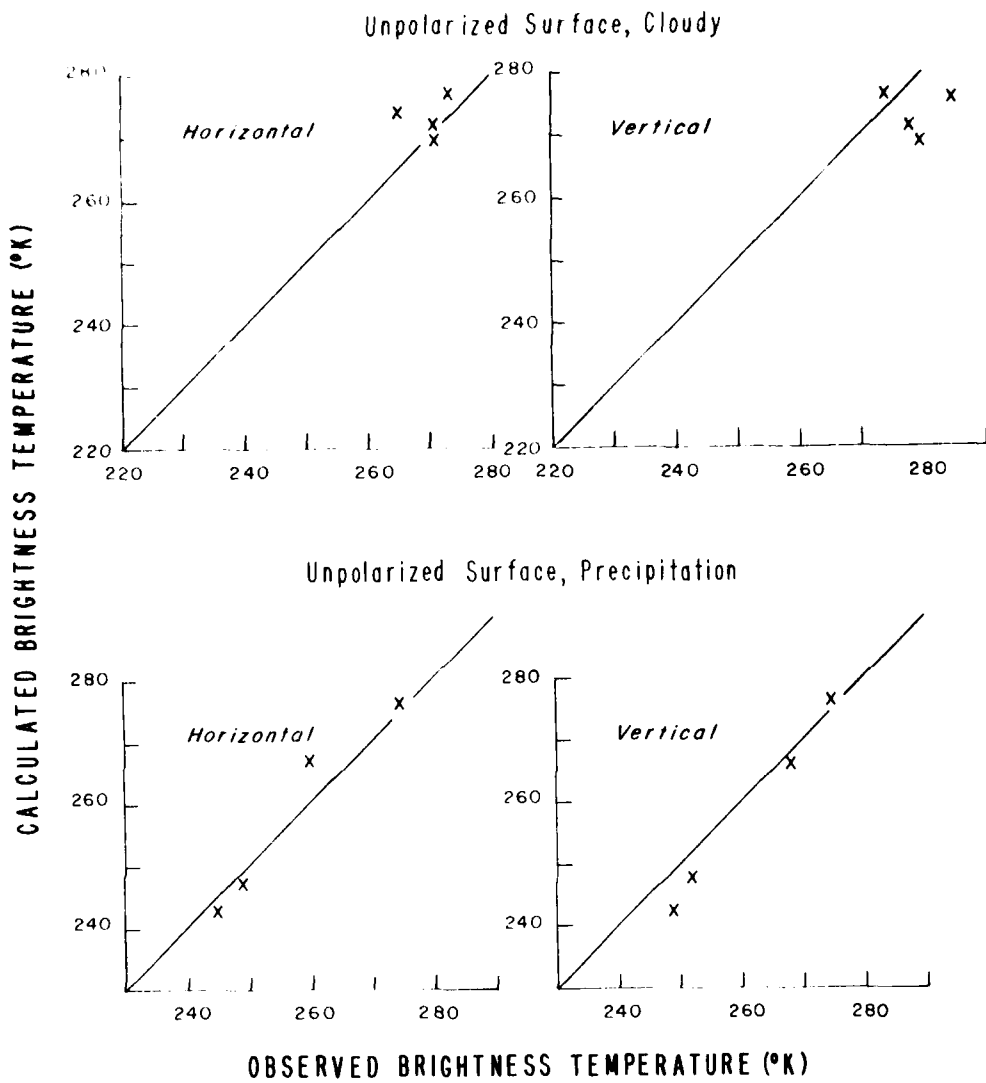


Fig. 2.5. Same as Fig. 2.4, except for cloudy and precipitation cases.

program correctly show the characteristics of polarization for the cases employed. Among these cases, the computed horizontal and vertical brightness temperatures for Miami, and Key West, Florida, respectively, differ significantly (on the order of 10° K) from the observed value. The reason for the discrepancy is probably due to the sensitivity of the ESMR data on the surface characteristics. The footprints corresponding to the observed data chosen cover both land and water surfaces. Hence, the emissivities derived from Fresnel's reflection coefficients are probably not representing the actual surface characteristics which will be greatly altered due to foam and roughness along the coastline. For those over unpolarized surfaces, comparison between the computed results and observed data show agreement within about 6° K. It may be concluded that the radiative transfer program developed in this study appears to be quite reliable despite the difficulty involved in the determination of the surface emissivity in all weather conditions.

2.4 Computational Results

2.4.1 Atmospheric profiles and cloud models. Two climatological profiles are used in the theoretical sensitivity study. The first profile is for the 30° N latitude, July and the second profile is for the midlatitude winter. For both profiles, temperature, water vapor concentration, and height values are interpolated to 40 standard pressure levels for computational purposes. The temperature and humidity profiles are shown in Fig. 2.6.

Based on the foregoing theoretical analyses, a microwave radiative transfer computer program for nonprecipitating and precipitating cloudy atmospheres was developed for both horizontal and vertical polarization components. The microwave radiative transfer program takes

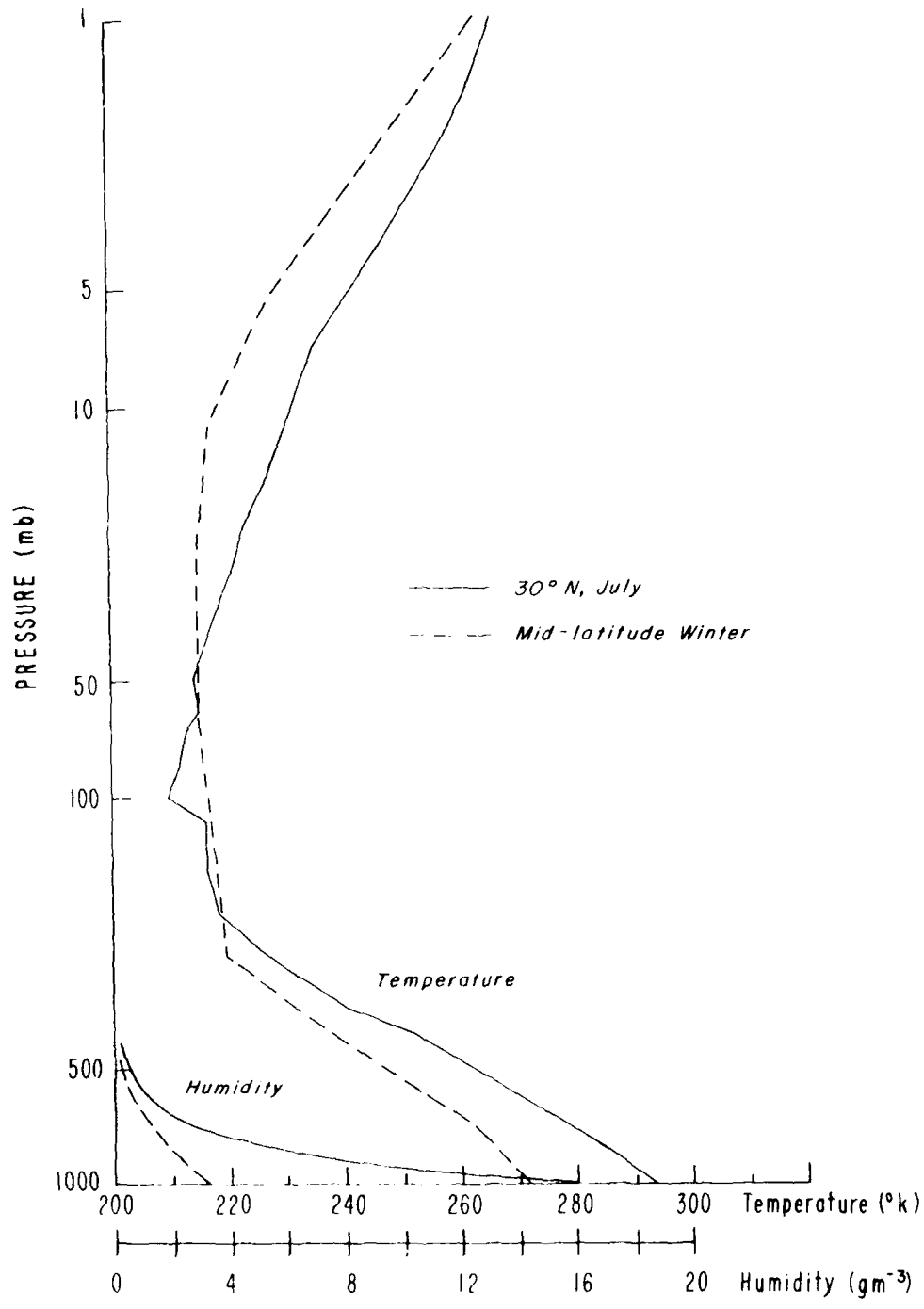


Fig. 2.6. Climatological temperature and humidity profiles for 30° N, July and Mid-latitude winter.

into consideration effects of the scattering and absorption properties of cloud particles and hydrometeors in a nonhomogeneous absorbing gaseous atmosphere. The single scattering parameters for the 37 GHz channel required for microwave radiative transfer calculations are obtained through a Mie scattering program for polydisperse spheres. The real and imaginary indices of refraction used are based on values given by Hollinger (1973) and were interpolated to the 37 GHz frequency.

A theoretical drop size distribution based on the rainfall rate given by Marshall-Palmer (1948) is used in the calculation. Rainfall rates of 1, 3, 5, 10, 15, 20, 25, and 30 mm/hr and cloud thicknesses of 1, 2, 3, 4, and 5 km are used in the sensitivity analysis. The cloud temperature is assumed to be the same as that of the surrounding air and a mean temperature value is taken in conjunction with the radiative transfer calculation. To carry out theoretical calculations over the land surface, an emissivity value of 0.96 is used for each discrete stream. For the water surface, the refractive index of the air-water interface depends on the temperature and salinity. Shown in Table 2.1 are emissivity values for a number of surface temperatures and salinities. Since variations in the emissivity value are quite small, we have assumed a temperature of 273° K and 35 PPT (percentage per thousand) salinity in the theoretical computations. Fig. 2.7 shows the degree of polarization over the water surface as a function of the incident (or emergent) angle. It is seen that there are differences in values between these cases but the polarization patterns are all quite similar. Over the water surface, the emissivity value for each discrete stream has been calculated by using Eqs. (2.49) - (2.51).

2.4.2 Unpolarized surface (over land). Brightness temperatures for both horizontal and vertical polarization components over the land surface as functions of the discrete zenith angle, and cloud thickness for

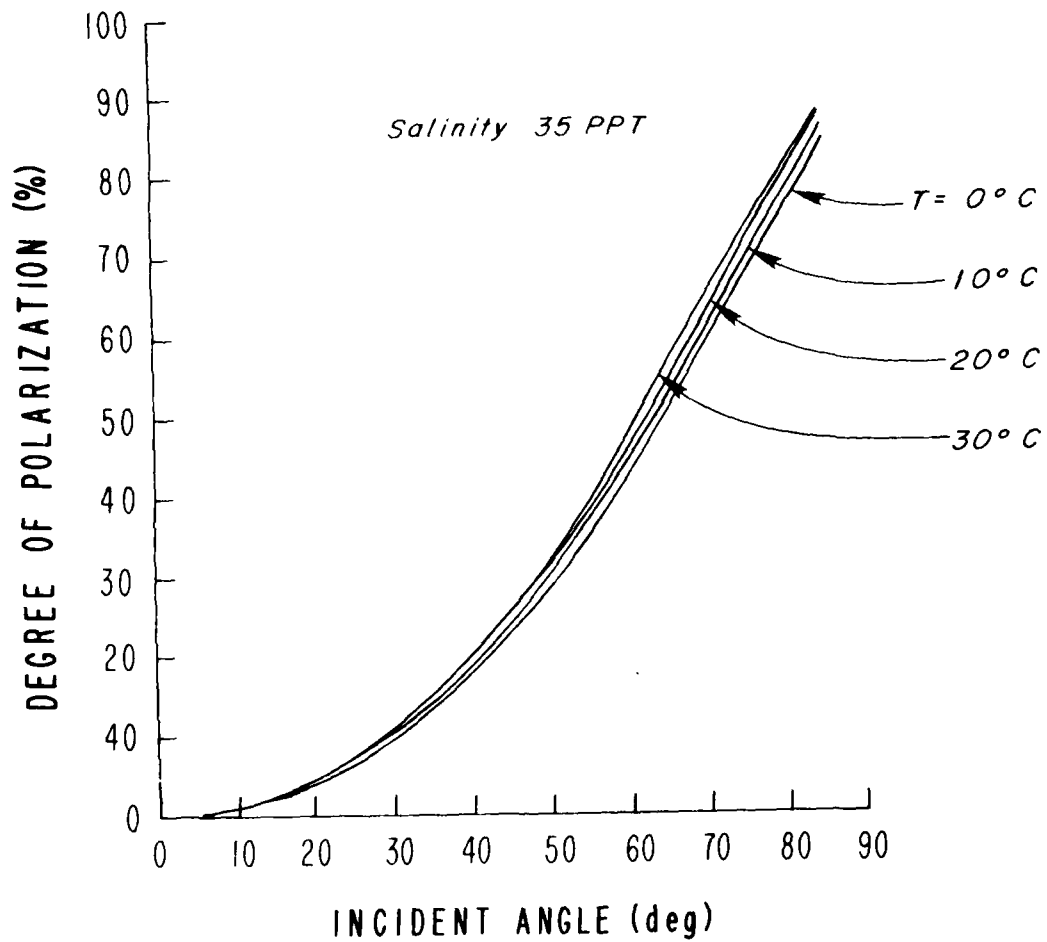


Fig. 2.7. Degree of linear polarization over the water surface as a function of the incident (emergent) angle.

Table 2.1. Emissivities over water surface at 50° incidence angle.

Temperature (°C)	Salinity PPT	Refractive Index m_r	Refractive Index m_i	Emissivity ϵ_h ϵ_v		Degree of Polarization (%)
0	35	3.8862	2.3838	0.3796	0.6811	28.90
10	35	4.3893	2.6158	0.3495	0.6502	30.08
20	35	4.9625	2.7670	0.3256	0.6181	30.99
30	35	5.4878	2.7849	0.3105	0.5972	31.58
0	0	3.8572	2.3189	0.3853	0.6951	28.67
0	10	3.8748	2.3810	0.3802	0.6889	28.87
0	20	3.8848	2.3844	0.3796	0.6882	28.90
0	30	3.8875	2.3848	0.3795	0.6398	25.54

rainfall rates are of 1 and 10 mm/hr displayed in Fig. 2.8 and 2.9.

The temperature and humidity profiles for 30° N latitude, July and an emissivity value of 0.96 for each discrete-stream were used in the theoretical calculations. Brightness temperatures emerging from the rain clouds over land surface show weak polarization as evident in these figures. Moreover, it is seen that the brightness temperature decreases as the cloud thickness and rainfall rate increase. Clearly, over land surfaces, the total liquid water content in the atmosphere reduces the upwelling brightness temperature.

Figure 2.10 depicts variations of the brightness temperature at 50° incidence angle emerging from the top of the atmosphere as functions of the cloud thickness and rainfall rate. Brightness temperatures decrease when the cloud thickness increases as pointed out previously. When the rainfall rate is less than about 5 mm/hr, brightness temperatures decrease drastically as rainfall rates increase for all five cloud

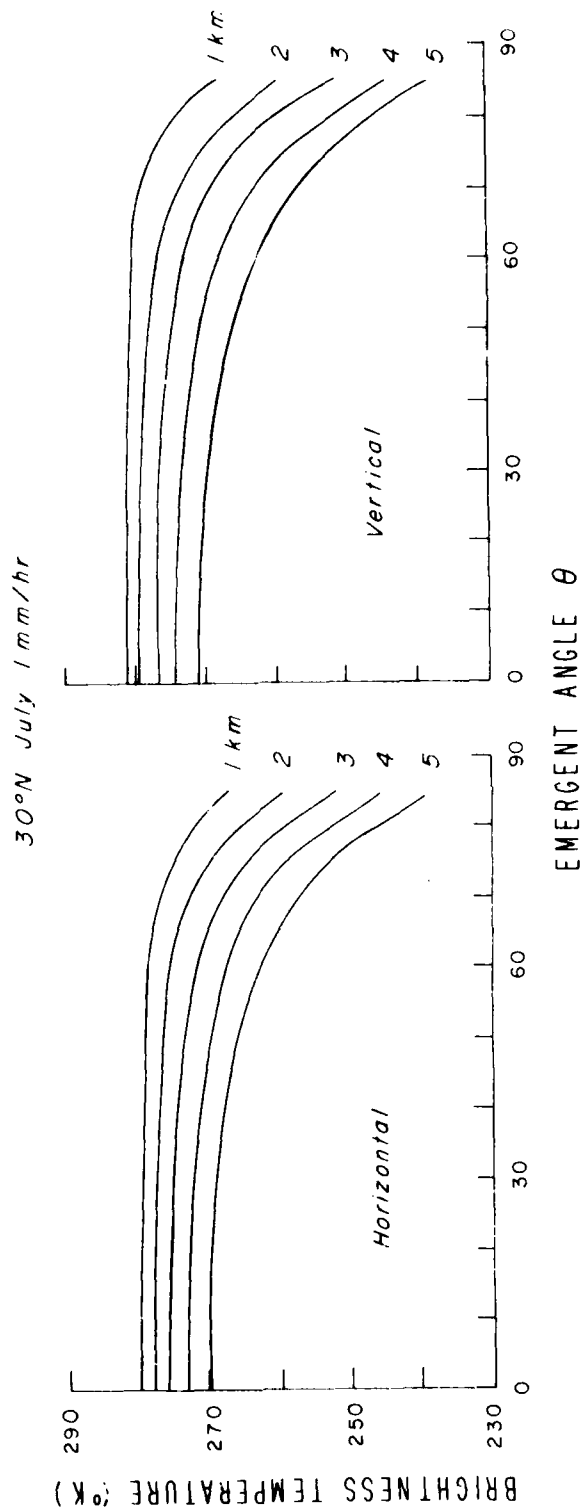


Fig. 2.8. Brightness temperatures for both horizontal and vertical polarization components over land surface as functions of the emergent (incident) angle and five cloud thicknesses using a 30° N, July, profile for a 1 mm/hr rainfall rate.

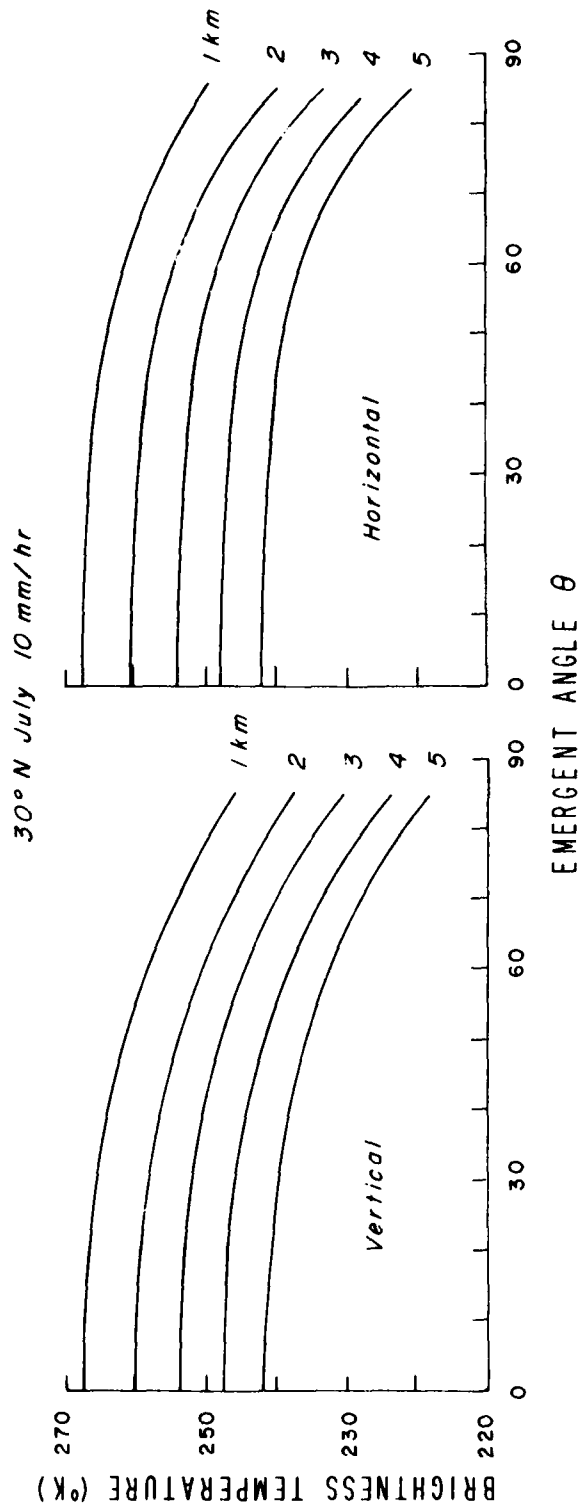


Fig. 2.9. Same as Fig. 2.8, except for a 10 mm/hr rainfall rate.

30° N July $\theta = 50^\circ$

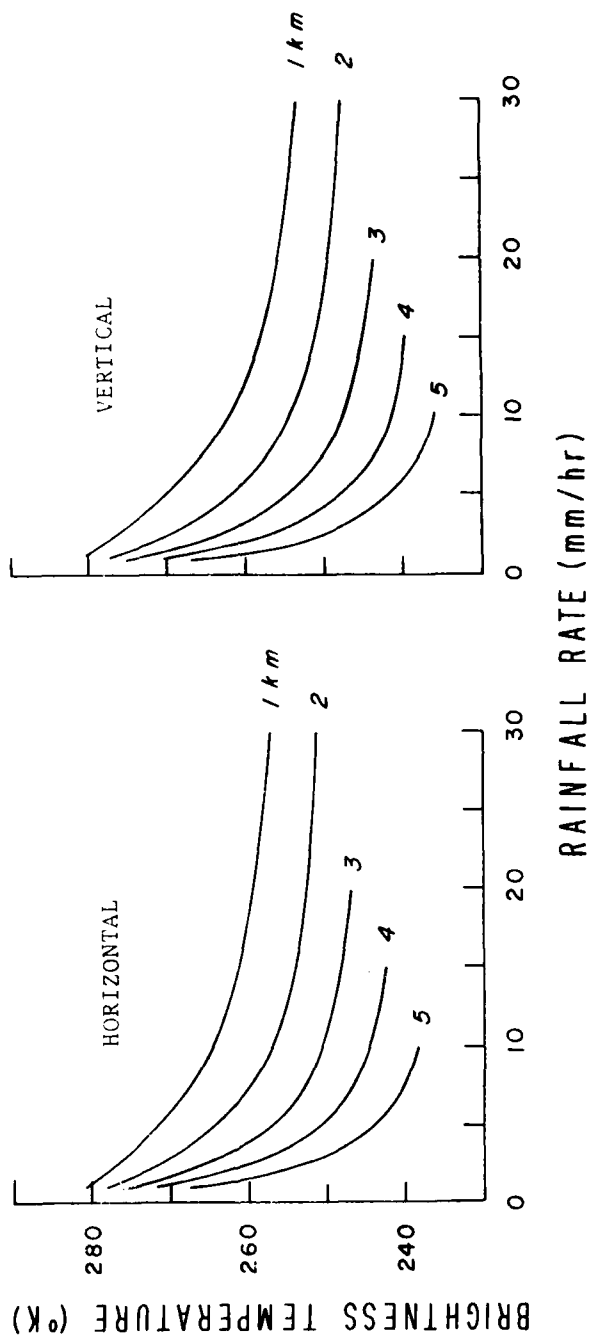


Fig. 2.10: Brightness temperatures at an emergent angle of 50° as functions of the rainfall rate for five cloud thicknesses and for a 30° N, July, profile over land. The lower rainfall rates used for 3 - 5 km cloud thickness cases are computational limitations permitted in the transfer program (see also Figs. 2.17 - 2.19).

thicknesses. The decrease is much more pronounced for thicker clouds. We see that brightness temperatures do not change significantly when the rainfall rate is greater than 5 mm/hr. The reason that the brightness temperature decreases when the rainfall rate increases is due to the progressively stronger backscattering by large raindrops. Note that in reality thin clouds normally do not produce high rainfall rates.

2.4.3 Polarized surface (over calm water). In this subsection, we report the resulting calculations which were carried out for polarized surfaces. Let the horizontal and vertical brightness temperatures be T_B^H and T_B^V , respectively and define the degree of linear polarization as follows:

$$P(\%) = \frac{T_B^V - T_B^H}{T_B^V + T_B^H} \times 100\% \quad (2.53)$$

The polarized emissivities used in the transfer calculation were derived from Eqs. (2.49) - (2.51) using the index of refraction corresponding to a temperature of 273° K and a salinity of 35 PPT. Emissivity values as functions of the incident (or emergent) angle for both horizontal and vertical components are shown in Fig. 2.11. The surface polarization varies from 0% at the 0° incident angle to 90% at the limb.

In Figs. 2.12 and 2.13 are shown both vertical and horizontal polarization components over the water surface as functions of the incidence angle using a 30° N, July, profile for 1 and 10 mm/hr rainfall rate. The brightness temperature patterns over polarized surfaces show significant differences from those over unpolarized surfaces.

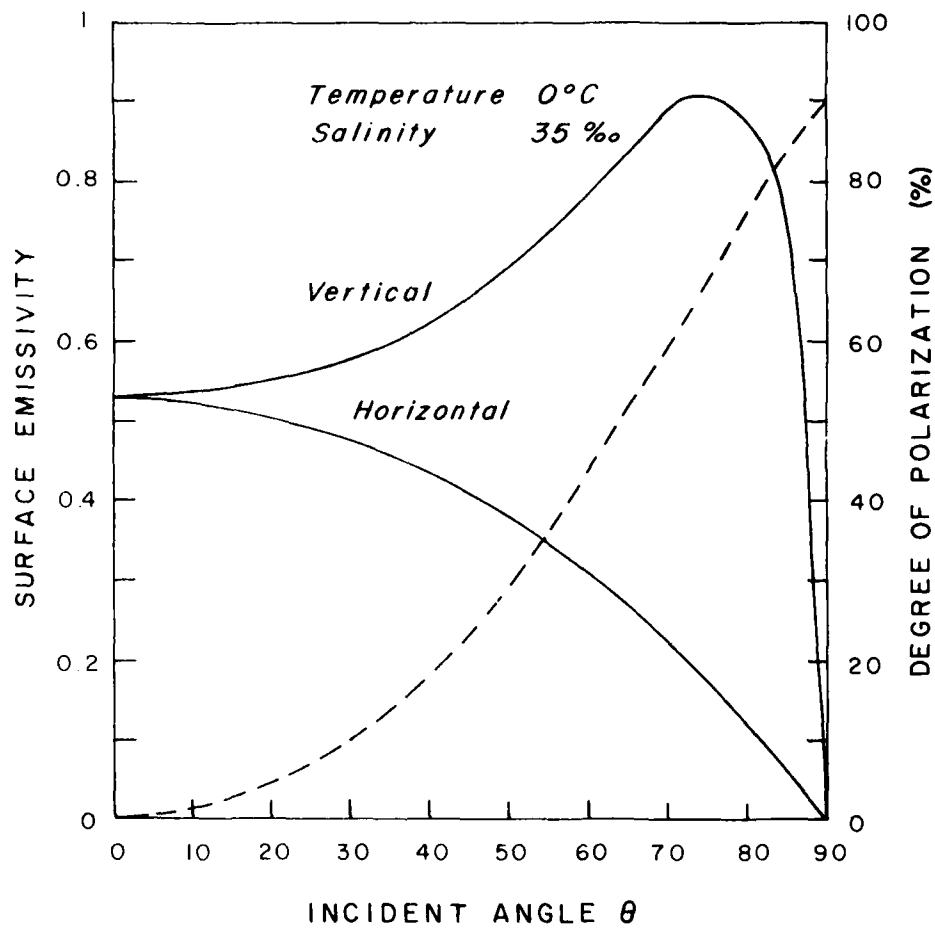


Fig. 2.11. Surface emissivity for vertical and horizontal components and degree of polarization as functions of the incident angle.

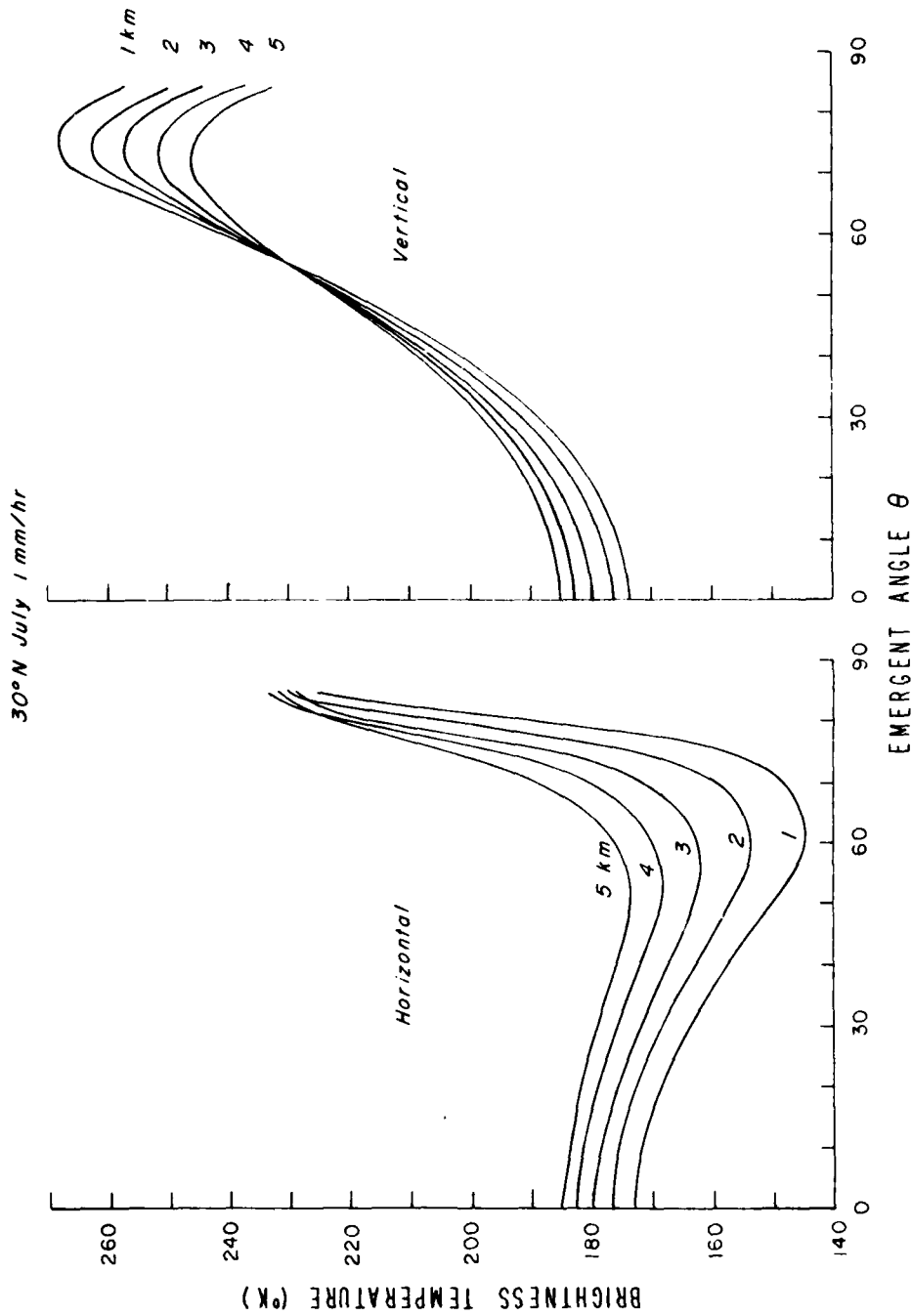


Fig. 2.12. Brightness temperatures for both horizontal and vertical polarization components over ocean surface as functions of the emergent angle and five cloud thickness using a 30° N, July, profile for a 1 mm/hr rainfall rate.

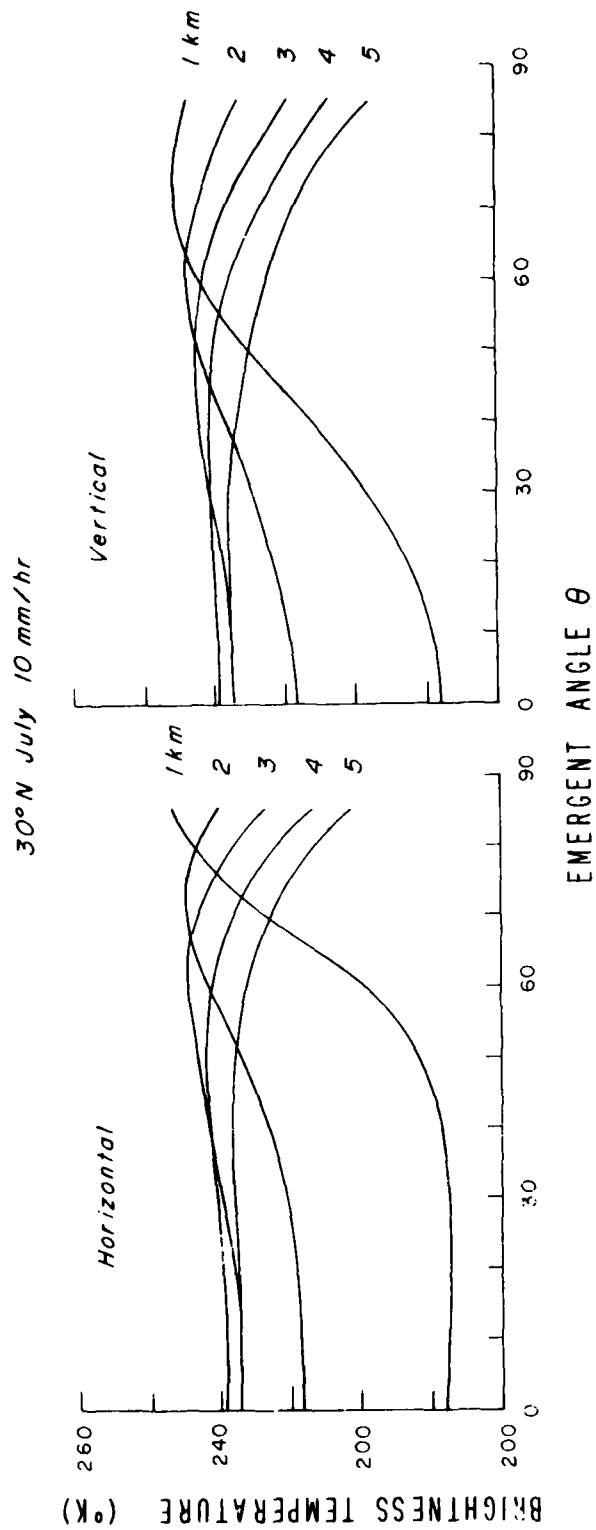


Fig. 2.13. Same as Fig. 2.12, except for a 10 mm/hr rainfall rate.

Significant differences between horizontal and vertical components at the top of the atmosphere can be seen for low rainfall rates and thin clouds over the water surface. Moreover, increasing the rainfall rate and cloud thickness, the brightness temperature increases for emergent angles less than about 60° owing to the larger cloud emissivity as compared with the surface emissivity. The polarization characteristics of the underlying surface are found to have little effect on the emergent brightness temperature for high rainfall rates. For a rainfall rate of 1 mm/hr, each cloud model produces quite different brightness temperature distribution between two polarization components, especially for the 1 km cloud case. High degree of polarization is seen to be located between $40^\circ - 70^\circ$ incidence angles (Fig. 2.14). As the cloud becomes thicker, polarization is found to be greatly reduced. In Figs. 2.15 and 2.16, brightness temperatures emergent from a midlatitude winter atmosphere are illustrated. In general, the brightness temperature patterns for vertical and horizontal components are found to resemble those from a 30° N, July, profile. As can be seen in Fig. 2.14, the emergent polarization values for two different profiles are rather close. Apparently, effect of the atmospheric temperature profile on the emergent polarization pattern appears to be minimum.

Figures 2.17 and 2.18 show the variation of the brightness temperature at the top of the atmosphere as a function of the rainfall rate for the 30° N, July, and midlatitude winter profiles, respectively. Both figures reveal quite different results from those over the unpolarized surface. For a given cloud thickness, the brightness temperatures for both polarization components increase with increasing rainfall

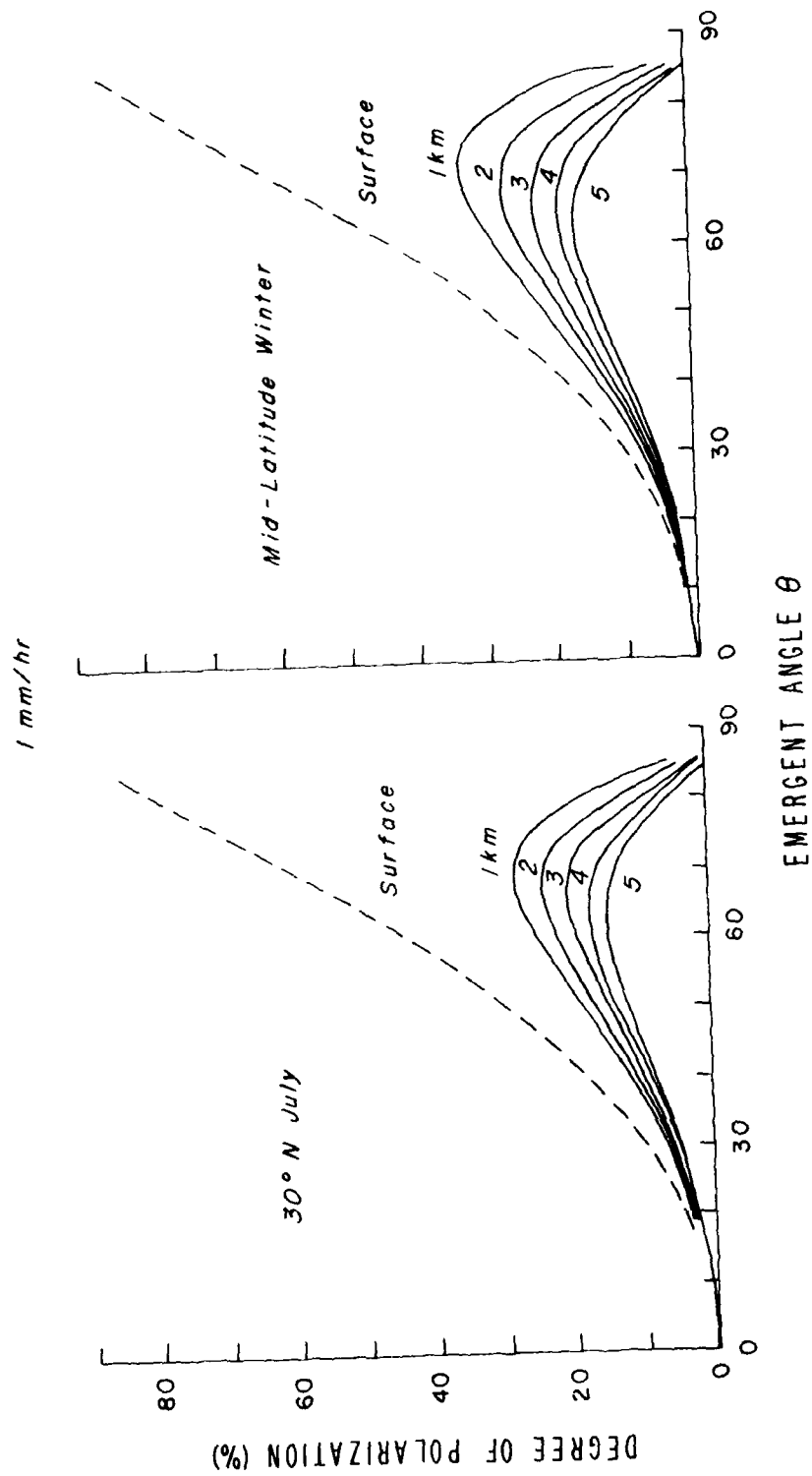
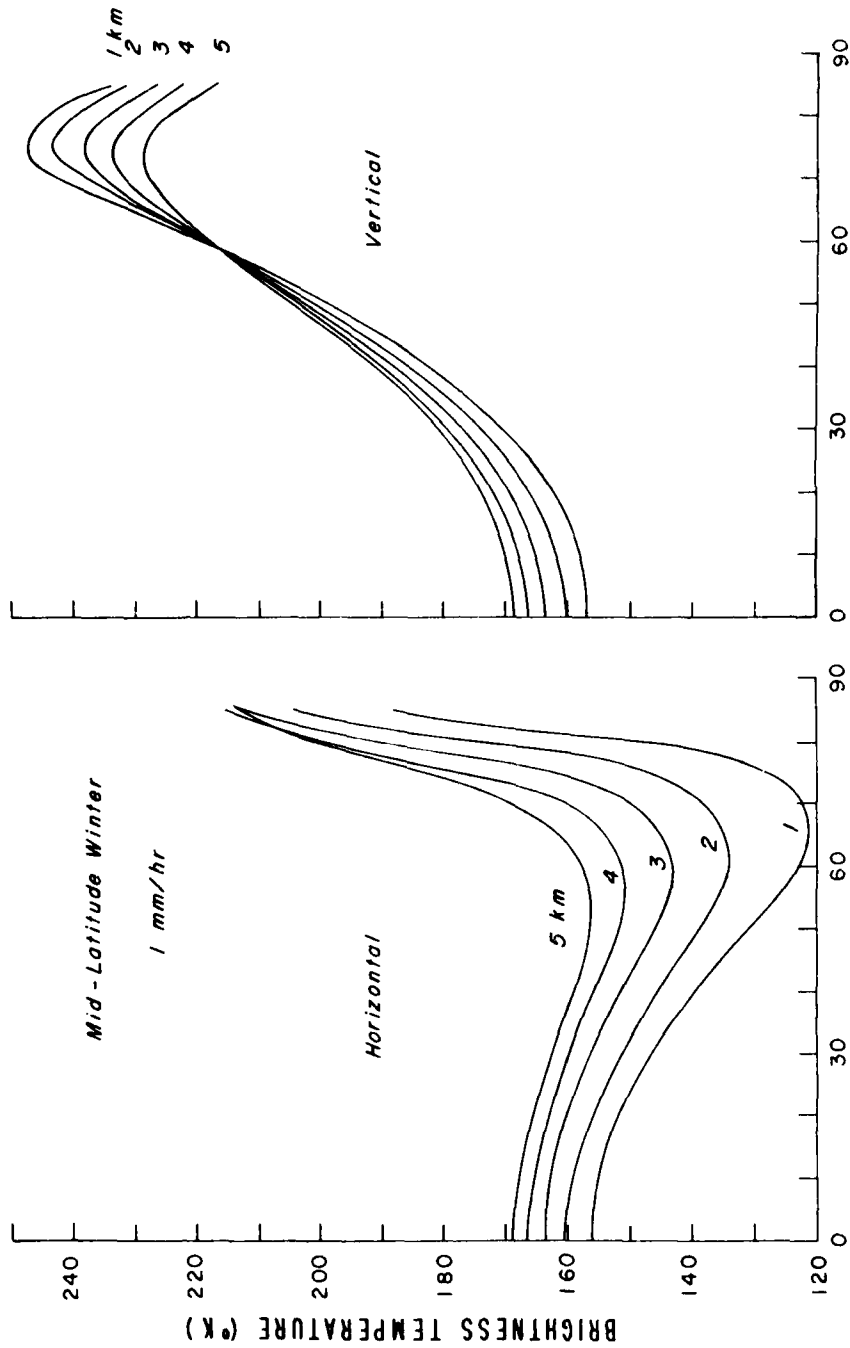


Fig. 2.14. Degree of polarization as a function of emergent angle for five cloud thicknesses having a rainfall rate of 1 mm/hr.



EMERGENT ANGLE θ

Fig. 2.15. Same as Fig. 2.12, except using a Mid-latitude winter profile.

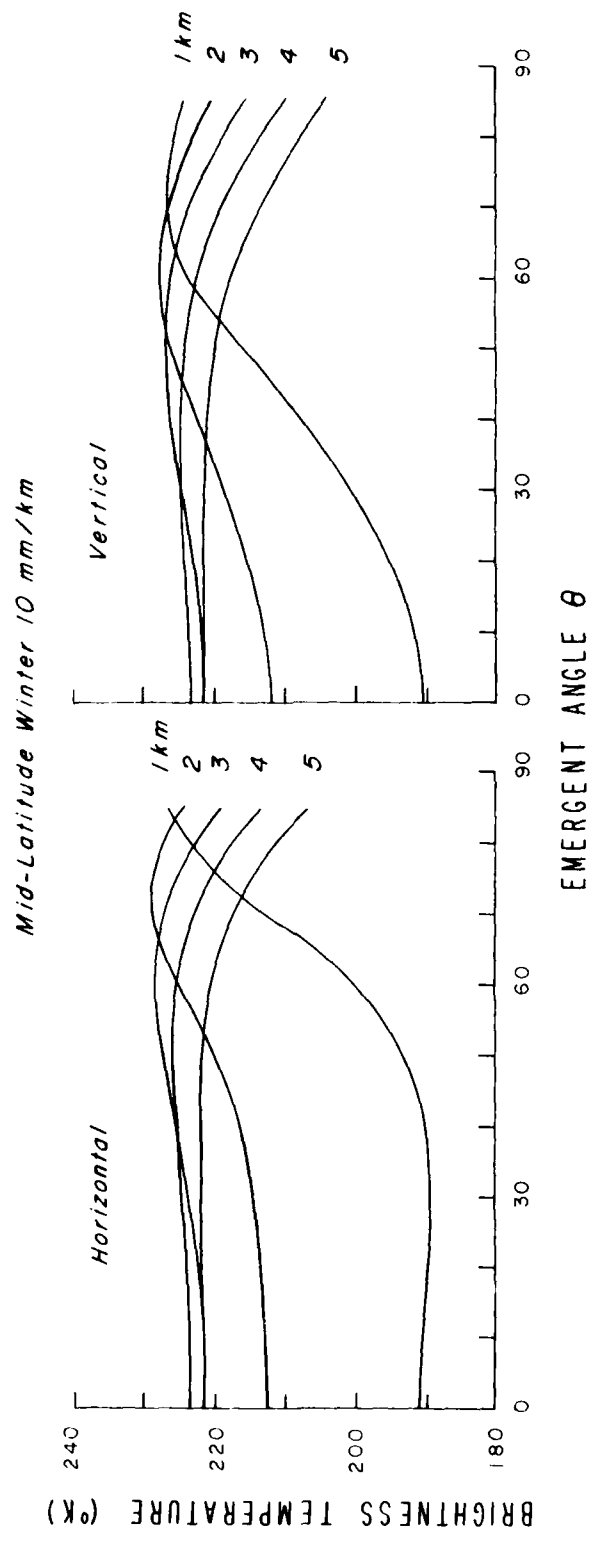


Fig. 2.16. Same as Fig. 2.15, except for a 10 mm/hr rainfall rate.

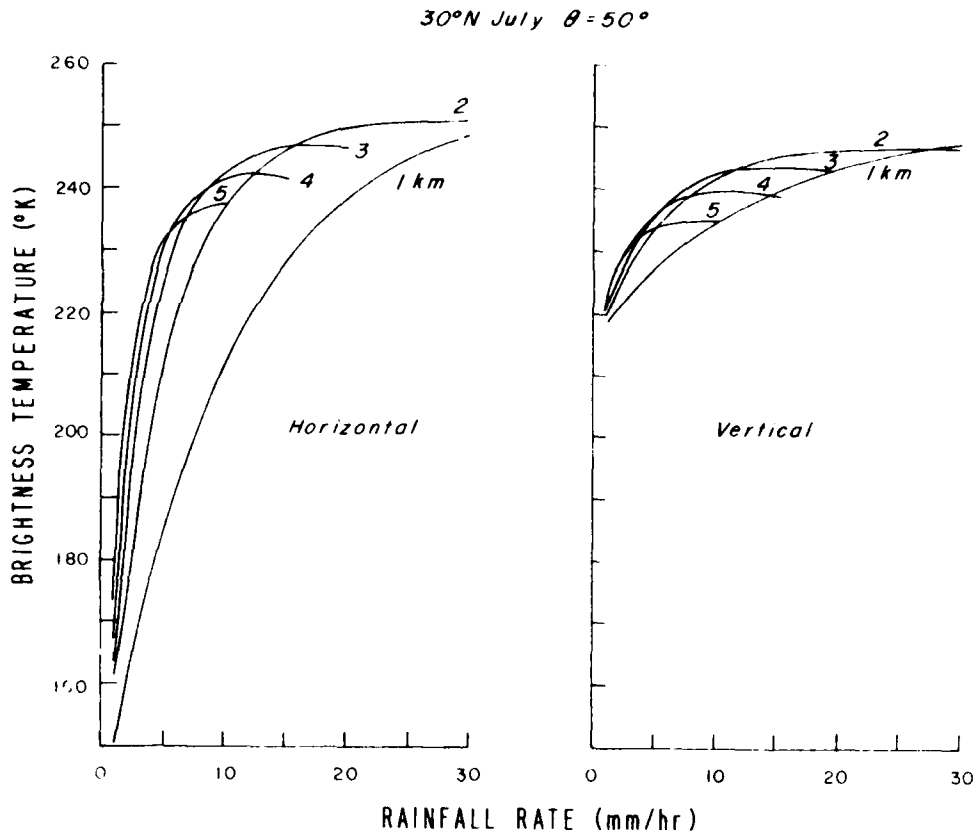


Fig. 2.17. Brightness temperatures at an emergent angle of 50° as functions of the rainfall rate for five cloud thicknesses and for a 30° N, July, profile over ocean.

Mid-Latitude Winter $\theta = 50^\circ$

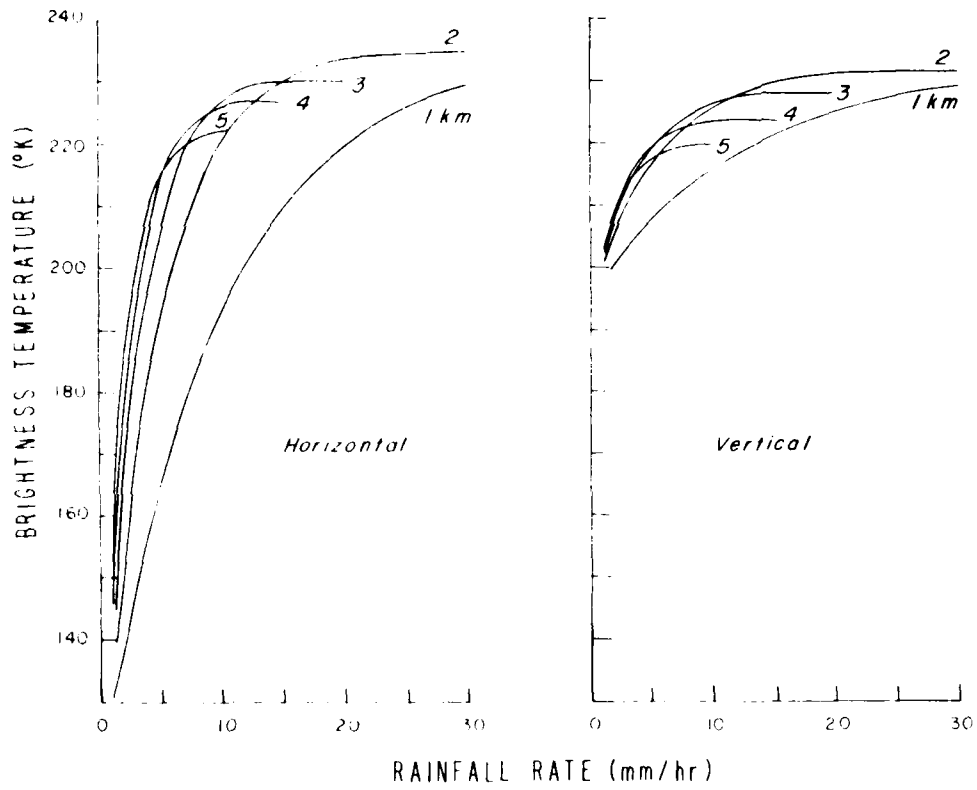


Fig. 2 18. Same as Fig. 2.17, except for a Mid-latitude winter profile.

rate. The horizontal component increases more rapidly as the rainfall rate increases. For a 1 km thick cloud, the difference between rainfall rates of 1 mm/hr and 3 mm/hr is 30° K, but it is only 3° K between 25 mm/hr and 30 mm/hr. For the vertical component we see a 5° K difference between 1 mm/hr and 3 mm/hr rainfall rates. Comparing the brightness temperatures for cloud thicknesses 1 and 5 km, it is seen that the difference between 1 mm/hr and 3 mm/hr is 20° K for a 1 km thick cloud, whereas it is 44° K for a 5 km thick cloud for the horizontal component. Only 5° K and 9° K differences, respectively, are observed for the vertical component. Fig. 2.19 illustrates the degree of linear polarization as a function of the rainfall rate for the two atmospheric profiles at an incident angle of 50°. The polarization patterns are fairly similar for the two different profiles. Degree of polarization at this angle is seen to be reduced as the rainfall rate and cloud thickness increase. That is that the total liquid water content within the atmosphere has a profound effect on the emergent polarization configuration at the 37 GHz frequency. In a cloudy or precipitating atmosphere, which is over a water surface, the emergent polarization varies from 0% to about 20%. Because of these variations, it seems possible to derive information of the cloud thickness and rainfall rate (or liquid water content) over water surfaces from vertical and horizontal polarization components. The relationship between the rainfall rate and liquid water content is illustrated in Table 3.1.

2.5 Liquid Water Content and Cloud Thickness Determination from ESMR 37 GHz Channel

On the basis of the theoretical analysis, it appears quite

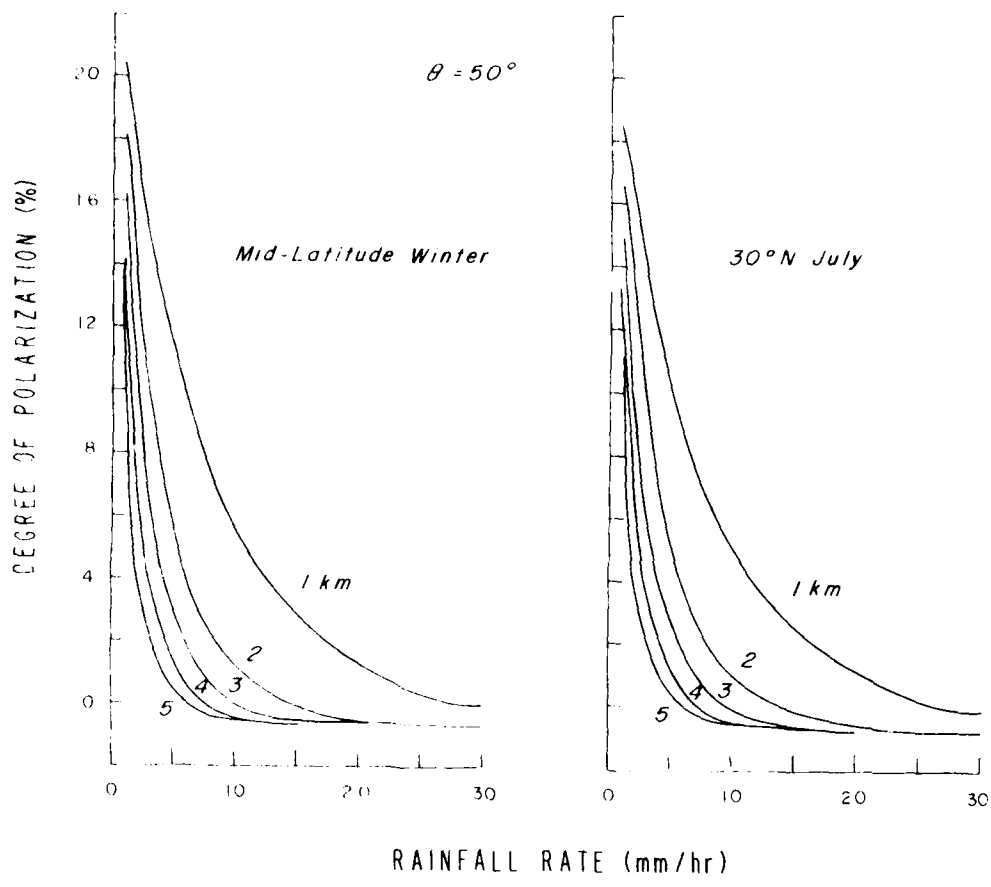


Fig. 2.19. Degree of polarization at an emergent angle of 50° as a function of rainfall rate and cloud thickness over ocean.

clear that the cloud thickness and rainfall rate (or liquid water content) in the atmosphere must be related to the emergent vertical and horizontal brightness temperatures. The functional relationship between the brightness temperatures and cloud parameters may be rather involved and complicated. However, in an attempt to understand how well the 37 GHz polarization data could be used for the quantitative inference of cloud and precipitation properties over ocean surfaces, it is assumed that

$$\left. \begin{aligned} T_B^V &= a_0 + a_1 \Delta Z + a_2 \Delta W \\ T_B^H &= b_0 + b_1 \Delta Z + b_2 \Delta W \end{aligned} \right\}, \quad (2.53)$$

where a_i and b_i ($i=0,1,2$) are certain relevant constants. It follows that

$$\left. \begin{aligned} \Delta W &= w_0 + w_1 T_B^H + w_2 T_B^V \\ \Delta Z &= z_0 + z_1 T_B^H + z_2 T_B^V \end{aligned} \right\}, \quad (2.54)$$

where w_i and z_i ($i=0,1,2$) are coefficients to be determined through theoretical-empirical procedures.

A three-dimensional linear regression program was utilized to determine the coefficients w_i and z_i denoted in Eqs. (2.53) and (2.54) over calm water surfaces. A total of 31 atmospheric cases were used for 30° N July and midlatitude winter profiles separately to compute brightness temperatures using the microwave radiative transfer program described

in the previous sections. Different liquid water content and cloud thickness were inserted into the atmosphere to obtain their relationship with the computed brightness temperatures T_B^H and T_B^V . The empirically derived coefficients based on the theoretical data are listed in Table 2.2.

In order to examine the validity of the empirical formulas, a number of theoretically computed brightness temperatures were used to retrieve the liquid water content and cloud thickness. The true and retrieved values are listed in Table 2.3 along with the brightness temperatures. For large liquid water content, the retrieved results appear to be within the acceptable range. For small liquid water content, negative values are obtained through the simple empirical equations. In view of the extreme difficulties encountered in the sounding of cloud parameters from satellites, the retrieved results derived from the theoretical-empirical analysis seems encouraging.

Thus, we have selected a number of ESMR data over ocean areas to test this technique for the cloud parameter inference. The ESMR data chosen cover mainly the area 20-25° N and 70-80° W for August 25 cases and 20-25° N and 80-85° W for February 20 cases described in a report by Astling and Liou (1979). The areas under consideration on these days had significant cloud cover. Results of the retrieved liquid water content and cloud thickness are tabulated in Table 2.4. In these exercises, empirical equations derived from the 30° N, July and midlatitude winter profiles were utilized for August and February cases, respectively. Results are surprisingly reasonable, except for a thin cloud case where a negative liquid water content is obtained. However, because of

Table 2.2 Empirical coefficients for the determination of liquid water content and cloud thickness over water surfaces.

Profile	w_0	w_1	w_2	z_0	z_1	z_2
30° N, July	1.0428	6.4866 $\times 10^{-3}$	-9.8447 $\times 10^{-3}$	1.3747 $\times 10^2$	1.6896 $\times 10^{-1}$	-5.9171 $\times 10^{-1}$
Midlatitude winter	1.0850	6.9790 $\times 10^{-3}$	-10.7565 $\times 10^{-3}$	1.1770 $\times 10^2$	2.3442 $\times 10^{-1}$	-7.4291 $\times 10^{-1}$

the lack of surface weather observations over ocean, it is not possible to verify the degree of reliability of these retrieval analyses. Certainly, remote sensing techniques developed for the cloud inference require proper verification from simultaneous in-situ aircraft cloud physics measurements and surface observations.

Table 2.3. Hypothetical analyses for the cloud liquid water content and thickness retrieval; (a) 30° N, July profile, and (b) midlatitude winter profile.

(a)					
Actual		Brightness Temperature (°K)		Retrieved	
ΔW (gm/cm ²)	ΔZ (km)	H	V	ΔW (gm/cm ²)	ΔZ (km)
0.02668	3	163.17	220.61	-0.0707	2.10
0.02238	1	169.04	223.20	-0.0580	1.55
0.06874	2	210.02	233.47	0.1066	2.39
0.30766	5	237.37	234.74	0.2715	6.26
0.34002	4	241.75	238.74	0.2606	4.64
0.33043	3	246.16	242.96	0.2477	2.88
(b)					
0.02668	3	146.01	202.29	-0.0719	1.65
0.02238	1	149.80	203.67	-0.0603	1.51
0.06874	2	193.33	216.54	0.1050	2.15
0.30766	5	221.73	219.28	0.2737	6.78
0.34002	4	226.25	223.40	0.2606	4.75
0.33043	3	230.63	227.63	0.2461	2.66

Table 2.4. Retrieved liquid water content and cloud thickness for (a) August 25 cases, and (b) February 20 cases

(a)					
Location		Observed		Retrieved	
Lat. (°N)	Long. (°W)	Brightness H	Temperature (°K) V	ΔW (gm/cm ²)	ΔZ (km)
22.8	80.3	192	223	0.0928	5.54
22.8	83.6	180	221	0.0347	4.70
22.8	80.5	189	219	0.1127	7.40
22.8	79.8	174	219	0.0154	4.87
21.6	79.8	169	217	0.0027	5.21
19.5	79.3	172	213	0.0615	8.08
(b)					
22.2	81.0	155	200	0.0154	5.46
22.1	84.4	170	208	0.0341	3.03
23.8	81.5	169	206	0.0486	4.28
23.8	81.9	166	204	0.0492	5.06
43.6	86.5	145	202	-0.0759	1.63

SECTION 3

EXPLORATION OF CLOUD PARAMETER INFERENCE FROM A COMBINATION OF INFRARED AND MICROWAVE CHANNELS

3.1 Parameterization of Infrared Radiative Transfer for a Two-Layered Cloud System

In the infrared $15 \mu\text{m CO}_2$ region, the upwelling radiance in a cloud-free atmosphere may be written as

$$I_{\bar{\nu}}(\infty) = B_{\bar{\nu}}(T_S)T_{\bar{\nu}}(\infty, 0) + \int_0^{\infty} B_{\bar{\nu}}[T(z)] K_{\bar{\nu}}(\infty, z) dz, \quad (3.1)$$

where $B_{\bar{\nu}}$ denote the Planck function at wavenumber $\bar{\nu}$, T_S the surface temperature, $T_{\bar{\nu}}$ the transmittance, and $K_{\bar{\nu}}$ the weighting function.

We first consider an overcast single cloud layer in the atmosphere. Since the cloud reflectivity is generally quite small in the infrared region (Liou et al., 1978; Hunt, 1973), the effect of cloud reflection may be ignored. Thus, the basic equation for the upwelling radiance may be written as

$$I_{\bar{\nu}}^C(\infty) = \{I_{\bar{\nu}}(z_c)T_{\bar{\nu}}^C(\Delta z) + \epsilon_{\bar{\nu}}^C B_{\bar{\nu}}[T(z_c)]\} T_{\bar{\nu}}(\infty, z_c) + \int_{z_c}^{\infty} B_{\bar{\nu}}[T(z)] K_{\bar{\nu}}(\infty, z) dz, \quad (3.2)$$

where z_c is the cloud top height, $T_{\bar{\nu}}^C$ and $\epsilon_{\bar{\nu}}^C$ represent the cloud transmissivity and emissivity, respectively, and $I_{\bar{\nu}}(z_c)$ is the upwelling radiance reaching the cloud bottom which is given by

$$I_{\nu}^{-}(z_c) = B_{\nu}^{-}(T_s) \tau_{\nu}^{-}(z_c, 0) + \int_0^{z_c} B_{\nu}^{-}[T(z)] K_{\nu}^{-}(z_c, z) dz . \quad (3.3)$$

In Eq. (3.2), the first term on the right hand side represents the radiance contribution from the atmosphere below the cloud, the second term is the contribution due to cloud emission, and the final term is the contribution of the gaseous emission from the atmosphere above the cloud. In Eq. (3.3), $\tau_{\nu}^{-}(z_c, 0)$ represents the clear column transmittance in reference to the cloud top height z_c . However, the clear column transmittance are normally available in reference to the top of the atmosphere; i.e. in the form of $\tau_{\nu}^{-}(\infty, 0)$. Hence, it is convenient to change the former transmittance to the latter form. According to the definition of the spectral transmittance, it is the ratio of the output radiance to the input radiance. Let the input radiance for the first layer be I_0 and the output radiance be I_1 , which is also the input radiance for the second layer. If the output radiance for the second layer is I_2 , then the transmittance of the combined layer, by definition, can be obtained from the product of the transmittance of the individual layer, i.e., $I_2/I_0 = (I_2/I_1)(I_1/I_0)$. On the basis of this physical argument, the transmittance at a given height below the cloud layer in reference to the top of the atmosphere may be expressed by

$$\tau_{\nu}^{-}(\infty, z) = \tau_{\nu}^{-}(\infty, z_c) \tau_{\nu}^{-}(z_c, z) .$$

Thus, the transmittance contained in the surface term of Eq. (3.3) may then be written as

$$T_{\nu}^{-}(z_c, 0) = T_{\nu}^{-}(\infty, 0) / T_{\nu}^{-}(\infty, z_c) , \quad (3.4)$$

and the weighting function is now given by

$$K_{\nu}^{-}(z_c, z) = \frac{\partial T_{\nu}^{-}(z_c, z)}{\partial z} = \frac{1}{T_{\nu}^{-}(\infty, z)} \frac{\partial T_{\nu}^{-}(\infty, z)}{\partial z} = \frac{1}{T_{\nu}^{-}(\infty, z)} K_{\nu}^{-}(\infty, z) . \quad (3.5)$$

For simplicity, $K_{\nu}^{-}(\infty, z)$ will be simply denoted as $K_{\nu}^{-}(z)$ in the following analysis. Upon substituting Eqs. (3.4) and (3.5) into Eq. (3.3) and Eq. (3.2), the upwelling radiance for an atmosphere containing a single cloud layer is now given by

$$I_{\nu}^{\mathcal{C}}(\infty) = T_{\nu}^{\mathcal{C}}(\Delta z) \{ B_{\nu}^{-}(T_s) T_{\nu}^{-}(\infty, 0) + \int_0^{z_c} B_{\nu}^{-}[T(z)] K_{\nu}^{-}(z) dz \} \\ + \epsilon_{\nu}^{\mathcal{C}}(\Delta z) B_{\nu}^{-}[T(z_c)] T_{\nu}^{-}(\infty, z_c) + \int_{z_c}^{\infty} B_{\nu}^{-}[T(z)] K_{\nu}^{-}(z) dz . \quad (3.6)$$

We now consider an atmosphere containing multiple cloud layers. Following the foregoing analyses for a single cloud layer, we let T_{ν}^{hc} and T_{ν}^{lc} denote the transmissivity and emissivity for high and low cloud, respectively. Then the upwelling radiance of an atmosphere with a high cloud layer can be written in a form similar to Eq. (3.2) as follows:

$$I_{\nu}^{\mathcal{C}}(\infty) = \{ T_{\nu}^{\text{hc}}(\Delta z_h) I_{\nu}^{-}(z_h) + \epsilon_{\nu}^{\text{hc}} B_{\nu}^{-}[T(z_h)] \} T_{\nu}^{-}(\infty, z_h) \\ + \int_{z_h}^{\infty} B_{\nu}^{-}[T(z)] K_{\nu}^{-}(\infty, z) dz , \quad (3.8)$$

where z_h and Δz_h are the high cloud top height and thickness, respectively. Assuming that there is a low cloud deck under the high cloud, then the upwelling radiance reaching the high cloud base is given by

$$I_{\nu}^{-}(z_h) = \{ I_{\nu}^{-}(z_{\ell}) \tau_{\nu}^{\lambda C}(\Delta z_{\ell}) + \tau_{\nu}^{\lambda C}(\Delta z_{\ell}) B_{\nu}^{-}[T(z_{\nu})] \} \tau_{\nu}^{-}(z_h, z_{\ell}) + \int_{z_{\nu}}^{z_h} B_{\nu}^{-}[T(z)] K_{\nu}^{-}(z_h, z) dz, \quad (3.9)$$

where z_{ν} and Δz_{ν} are the low cloud top height and thickness, respectively, and $I_{\nu}^{-}(z_{\nu})$, the upwelling radiance reaching the low cloud layer, is

$$I_{\nu}^{-}(z_{\nu}) = B_{\nu}^{-}(T_S) \tau_{\nu}^{-}(z_{\nu}, 0) + \int_0^{z_{\nu}} B_{\nu}^{-}[T(z)] K_{\nu}^{-}(z_{\nu}, z) dz. \quad (3.10)$$

Since the cloud reflection in the infrared $15 \mu\text{m CO}_2$ band is normally very small (see Liou et al, 1978), we may write

$$\tau_{\nu}^{\lambda C}(\Delta z_h) = 1 - \tau_{\nu}^{\lambda C}(\Delta z_h) \quad (3.11)$$

$$\tau_{\nu}^{\lambda C}(\Delta z_{\ell}) = 1 - \tau_{\nu}^{\lambda C}(\Delta z_{\ell})$$

Upon substituting Eqs. (3.10) and (3.11) into Eq. (3.9), we find

$$I_{\nu}^{-}(z_h) = \{ B_{\nu}^{-}(T_S) \tau_{\nu}^{-}(z_{\nu}, 0) + \int_0^{z_{\nu}} B_{\nu}^{-}[T(z)] K_{\nu}^{-}(z_{\nu}, z) dz \} \tau_{\nu}^{\lambda C}(\Delta z_{\ell}) \tau_{\nu}^{-}(z_h, z_{\ell}) + [1 - \tau_{\nu}^{\lambda C}(\Delta z_{\nu})] B_{\nu}^{-}[T(z_{\nu})] \tau_{\nu}^{-}(z_h, z_{\nu}) + \int_{z_{\nu}}^{z_h} B_{\nu}^{-}[T(z)] K_{\nu}^{-}(z_h, z) dz. \quad (3.12)$$

We then change the reference layer of clear column transmittances and weighting functions from high to low cloud layer to the top of the atmosphere as described previously to obtain

$$T_{\nu}^{-}(z_{\ell}, 0) = T_{\nu}^{-}(\infty, 0) / [T_{\nu}^{-}(\infty, z_h) T_{\nu}^{-}(z_h, z_{\ell})] ,$$

$$K_{\nu}^{-}(z_{\ell}, z) = K_{\nu}^{-}(\infty, z) / [T_{\nu}^{-}(\infty, z_h) T_{\nu}^{-}(z_h, z_{\ell})] , \quad 0 < z < z_{\ell} ,$$

$$K_{\nu}^{-}(z_h, z) = K_{\nu}^{-}(\infty, z) / T_{\nu}^{-}(\infty, z_h) , \quad z_{\ell} < z < z_h \quad (3.13)$$

Substituting Eq. (3.13) into Eq. (3.12) and subsequently into Eq. (3.8), we obtain the upwelling radiance emergent from a two-layer cloudy atmosphere in the form

$$\begin{aligned} I_{\nu}^{\uparrow C}(\infty) = & T_{\nu}^{\text{hc}}(\Delta z_h) T_{\nu}^{\ell C}(\Delta z_{\ell}) \{ B_{\nu}^{-}(T_s) T_{\nu}^{-}(\infty, 0) + \int_0^{z_c} B_{\nu}^{-}[T(z)] K_{\nu}^{-}(z) dz \\ & - B_{\nu}^{-}[T(z_{\ell})] T_{\nu}^{-}(\infty, z_{\ell}) \} + T_{\nu}^{\text{hc}}(\Delta z_h) \{ \int_{z_{\ell}}^{z_h} B_{\nu}^{-}[T(z)] K_{\nu}^{-}(z) dz \\ & + B_{\nu}^{-}[T(z_{\ell})] T_{\nu}^{-}(\infty, z_{\ell}) - B_{\nu}^{-}(z_h) T_{\nu}^{-}(\infty, z_h) \} + B_{\nu}^{-}[T(z_h)] T_{\nu}^{-}(\infty, z_h) \\ & + \int_{z_h}^{\infty} B_{\nu}^{-}[T(z)] K_{\nu}^{-}(z) dz . \end{aligned} \quad (3.14)$$

In the absence of high cloud, $T_{\nu}^{\text{hc}}(\Delta z_h) = 1$, and $z_h = z_{\ell}$, Eq. (3.14) reduces to

$$\begin{aligned}
I_{\nu}^{lc}(\dots) &= \tau_{\nu}^{lc}(\Delta z_{\ell}) \{ B_{\nu}(T_s) T_{\nu}^{-}(\dots, 0) + \int_0^{z_{\ell}} B_{\nu}[T(z)] K_{\nu}^{-}(z) dz \} \\
&+ [1 - \tau_{\nu}^{lc}(\Delta z_{\ell})] B_{\nu}(z_{\ell}) T_{\nu}^{-}(\dots, z_{\ell}) + \int_{z_{\ell}}^{\infty} B_{\nu}[T(z)] K_{\nu}^{-}(z) dz . \quad (3.15)
\end{aligned}$$

This is the upwelling radiance for the single-layer cloudy atmosphere.

Likewise, if the low cloud is absent, then Eq. (3.14) becomes

$$\begin{aligned}
I_{\nu}^{hc}(\dots) &= \tau_{\nu}^{hc}(\Delta z_h) \{ B_{\nu}(T_s) T_{\nu}^{-}(\dots, 0) + \int_0^{z_h} B_{\nu}[T(z)] K_{\nu}^{-}(z) dz \} \\
&+ [1 - \tau_{\nu}^{hc}(\Delta z_h)] B_{\nu}(z_h) T_{\nu}^{-}(\dots, z_h) + \int_{z_h}^{\infty} B_{\nu}[T(z)] K_{\nu}^{-}(z) dz . \quad (3.16)
\end{aligned}$$

In no cloud conditions, $\tau_{\nu}^{hc}(\Delta z_h) = \tau_{\nu}^{lc}(\Delta z_{\ell}) = 1$, and $z_h = z_{\ell} = 0$, Eq. (3.14) reduces to the expression for the clear column radiance denoted in Eq. (3.1). Eq. (3.14) is the fundamental parameterized transfer equation to be used for the inference of the cloud thickness, and high and low cloud top heights.

3.2 High and Low Cloud Top and Thickness Determination from HIRS Channels

3.2.1 Determination of cirrus cloud top height. In the following analysis, we replace ν by i to indicate the channel number in the $15 \mu\text{m}$ CO_2 band. Next we let the difference between the upwelling radiances for atmospheres containing no cloud and a single-layer high cloud layer be

$$\Delta A_i = I_i(\dots) - I_i^{hc}(\dots) . \quad (3.17)$$

Substituting Eqs. (3.1) and (3.16) into Eq. (3.17), we have

$$\Delta A_i = [1 - \tau_i^{hc}(\Delta z_h)] \{ B_i(T_s) T_i(\omega, 0) - B_i[T(z_h)] T_i(\omega, z_h) + \int_0^{z_h} B_i[T(z)] K_i(z) dz \} \quad (3.18)$$

To a good approximation, the cloud transmissivity may be considered to be independent of the channel number in the 15 μm interval (Liou, et al., 1978), i.e., $T_i^C(\Delta z) = T_j^C(\Delta z)$, where i and j are two adjacent channels in the 15 μm CO_2 band. Define the ratio of the radiance differences for i and j channels as follows:

$$G(z_h) = \frac{\Delta A_i}{\Delta A_j} = \frac{g_i(z_h) + \int_0^{z_h} B_i[T(z)] K_i(z) dz}{g_j(z_h) + \int_0^{z_h} B_j[T(z)] K_j(z) dz}, \quad (3.19)$$

where

$$g_k(z_h) = B_k(T_s) T_k(\omega, 0) - B_k[T(z_h)] T_k(\omega, z_h), \quad k=i, j.$$

Because of the ratio, the G function is independent of the cloud opacity, but depends only on the weighting function of the channel, the cloud height, and the radiance profile from the surface to the cloud top (McCleese and Wilson, 1976).

The G function has been evaluated based on Eq. (3.19) utilizing the channel pair (2,3), (3,4), (4,5), and (5,6) of the Nimbus 6 HIRS 15 μm band for two climatological temperature profiles. In Fig. 3.1,

solid and dashed lines are for mid-latitude summer and a tropical summer profile, respectively. It is seen that the G function is not strongly dependent on the atmospheric temperature profile up to the level of the tropopause. Inspection of Eq. (3.19) reveals that the G value depends only on z_h for a given radiance profile $B_{\nu}^{-}[T(z)]$. The G function normally varies insignificantly when the difference of the radiance profiles is not very pronounced. The relation between the G value and z_h may be constructed through a regression analysis. From the definition of the G function, the observed and clear column radiance values are required for the computation. These values may be evaluated from the observed temperature profile.

In Fig. 3.1, curves A, B, C, and D are for the channel pair (2,3), (3,4), (4,5), and (5,6), respectively for a mid-latitude summer profile. We find that the regions in which the cloud height z_h is a monotonic function of the G value are quite limited for curves A and B. We note that the spread of the G value is from 0.03 to 0.08, while z_h ranges from 10 to 12.8 km for curve A. This implies that for any G value outside the domain from 0.03 to 0.08, there will be no solution for z_h . Moreover, unless z_h is between 10 and 12.8 km, there also will be no solution for it. The region in which the G value increases with height is much wider for curves C and D. The G value ranges from 0.02 to 0.32 when z_h is between 2.4 and 12 km for curve C. The slope of the curve C is less sharp as compared with curves A and B. For this curve z_h is less affected by the change of the G value. This implies that the estimated z_h value is more tolerable to the observed error in the G value.

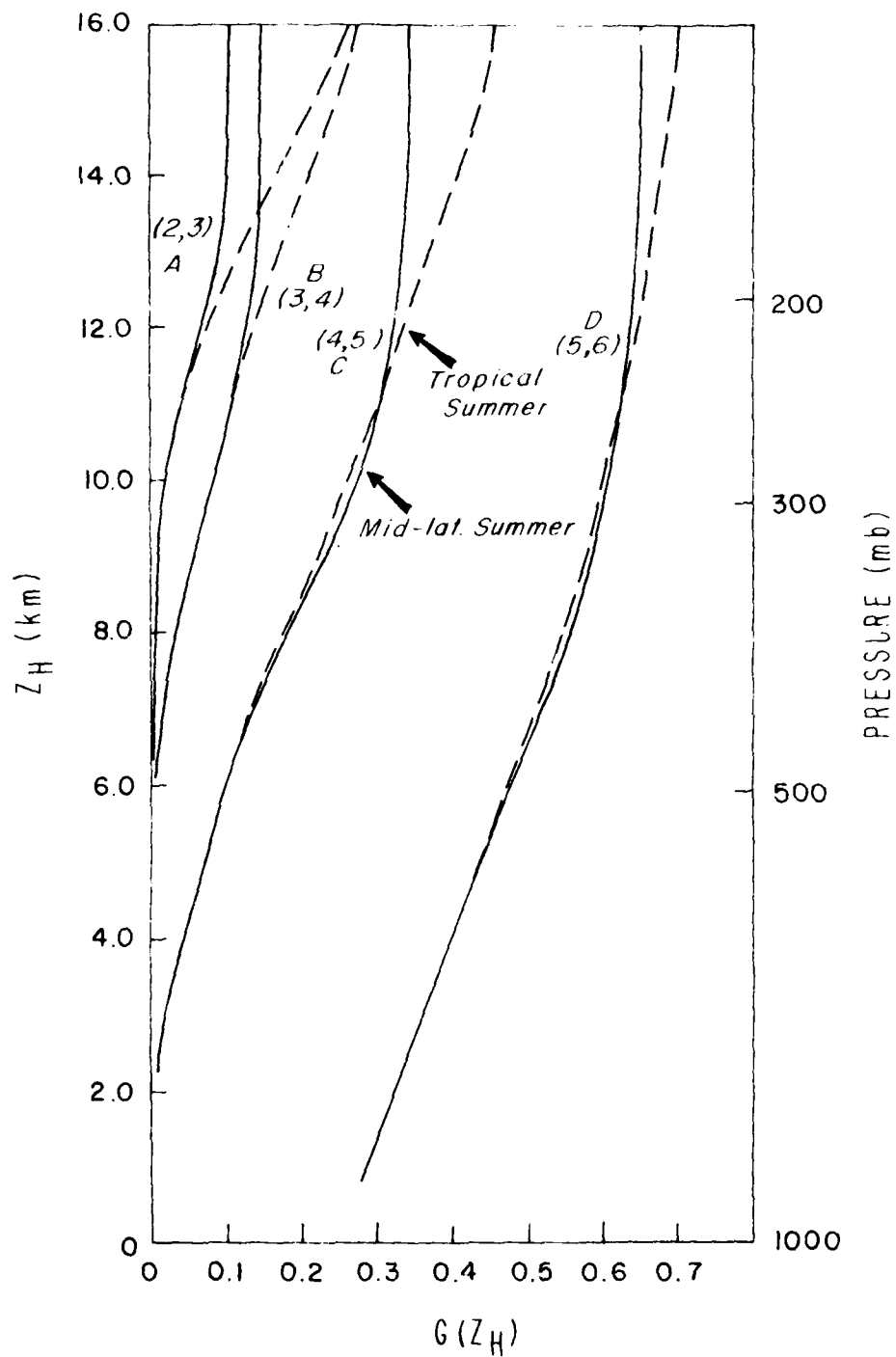


Fig. 3.1. The relationship between the G function (see text for the definition) and the high cloud top height for four channel pairs using two atmospheric profiles.

In view of the preceding consideration, we find that curves C and D are better options for the determination of the high cloud top height. Since channel 6 senses that the lower part of the atmosphere, the low cloud has a significant effect on the determination of the G value for the channel pair (5,6). In addition, the region for the curve D extends to only about 11 km. It follows that this channel pair is not ideal for estimating the high cloud top height.

For curve C which is constructed from channels 4 and 5, the cloud height z_h is approximately a linear function of G between 6 and 12 km. The height range is approximately the location of the cirrus cloud top. Thus, z_h may be determined by the following linear equation:

$$z_h = d_0 + d_1 G,$$

where the coefficients d_0 and d_1 are determined through a regression analysis.

3.2.2 Determination of cirrus cloud thickness. The HIRS water vapor channel in the 6.3 μm H_2O band is intended for the estimate of the water vapor concentration in the upper troposphere and the detection of thin cirrus. The weighting functions for the HIRS temperature and water vapor channels are shown in Fig. 3.2 (Smith et al., 1975). Examination of the weighting function of the 6.7 μm water vapor channel (channel 10) reveals that this channel peaks at about 400 mb and has very insignificant interference from the atmosphere below 700 mb. After the cloud top height is estimated from the previous analyses the cloud thickness also may be evaluated from the scheme described below.

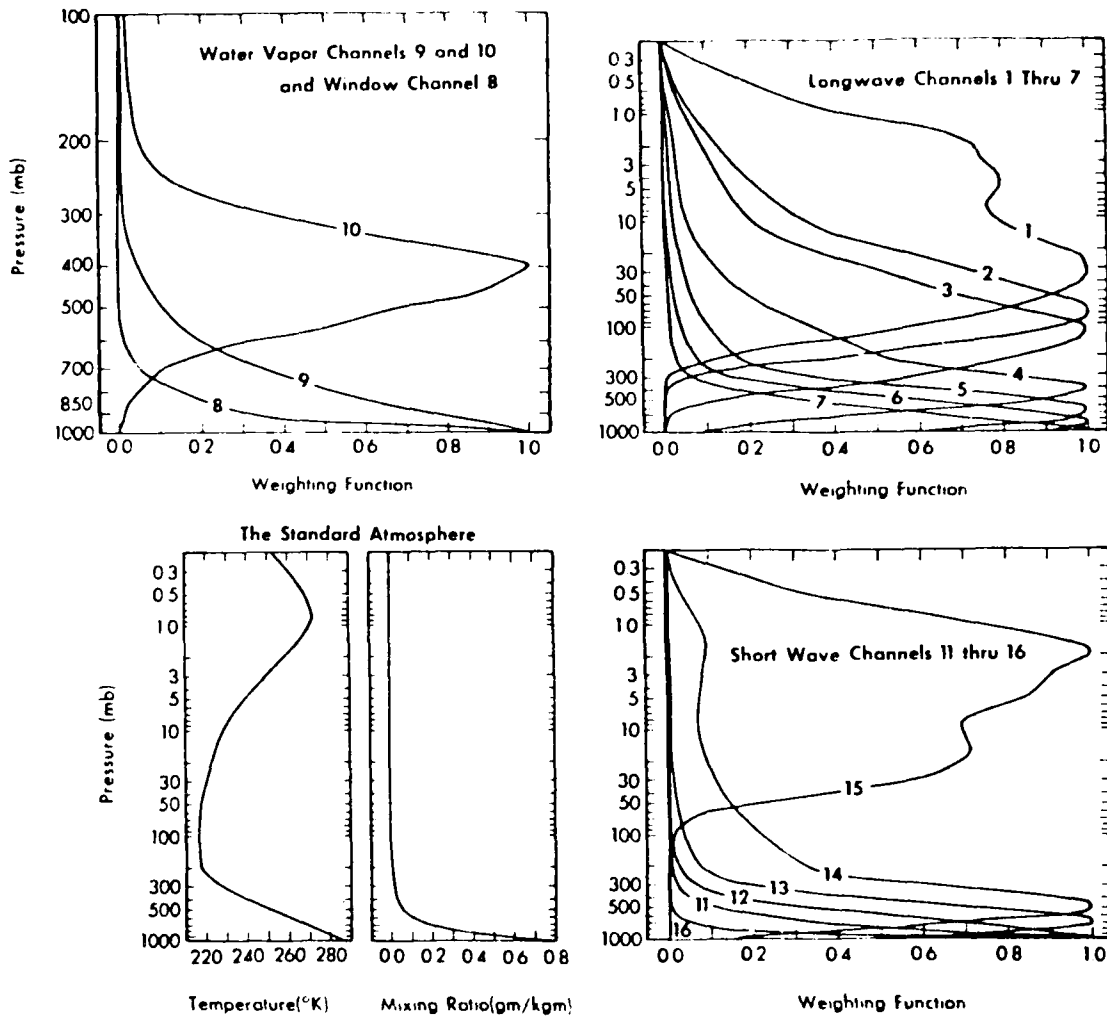


Fig. 3.2. Weighting Functions for the HIRS Temperature and Water Vapor Channels.

For a thin cirrus cloud, the cloud transmissivity may be approximately expressed as an exponential function of the cloud optical thickness. Since $\beta_e (\text{km}^{-1})$ is the total extinction of radiation due to absorption and scattering by the cloud particles, the geometric thickness $\Delta z (\text{km})$ is related to the optical depth by the equation

$$\Delta z = 1/\beta_e \cdot (\text{km}) \quad (3.20)$$

For the computation of β_e , the cirrus cloud was assumed to be composed entirely of ice. The single scattering computation was made for the central wavenumber 1508.29 cm^{-1} in the water vapor band utilizing a theoretical ice cloud model developed by Liou (1972). The major and minor axes of the cylinder used were 200 and 60 μm , respectively, with a concentration of 0.05 cm^{-3} . The real and imaginary parts of the index of refraction were taken from the measurement by Schaaf and Williams (1973). The value for β_e is 1.326 km^{-1} .

From Eq. (3.20), the transmissivity of a thin cirrus cloud may be expressed as

$$t_i^{hc} = \exp(-\beta_e \Delta z_h) \quad (3.21)$$

Upon substituting Eq. (3.21) in Eq. (3.16), the cirrus cloud thickness may be derived to give

$$\Delta z_h = -\frac{1}{\beta_e} \ln \left[\frac{\left[t_i^{hc}(\infty) - \beta_i(z_h) T_i(\infty, z_h) + \int_{z_h}^{\infty} \beta_i [T(z)] K_i(z) dz \right]}{\int_0^{z_h} \beta_i [T(z)] K_i(z) dz - \beta_i(z_h) T_i(\infty, z_h)} \right] \quad (3.22)$$

Because of the strong water vapor absorption in this channel, low clouds below 700 mb have little effect on the observed radiation at the satellite point. Thus, the upwelling radiance for the 6.7 μm H_2O channel is only affected by the high cloud. Consequently, the term I_i^{hc} in Eq. (3.22) may be considered as the satellite observed radiance. Since the cloud top height z_h has been estimated from the foregoing analysis, the cirrus cloud thickness Δz_h may be subsequently determined using Eq. (3.22).

3.2.3 Determination of low cloud top height. Examining the weighting function depicted in Fig. 3.2, we see that most of the energy contribution to the upwelling radiance for the 11 μm window channel (channel 8) comes from the atmosphere below 700 mb. If a low cloud has an optical depth large enough to be considered a blackbody radiator, then the total upwelling radiance at the window channel will arise from two energy sources; one is the gaseous emission of the clear atmosphere above the cloud top, while the other is the blackbody emission of the cloud layer. If the temperature profile and the average cloud temperature are known, then there should exist a simple relationship between the upwelling radiance and cloud top height.

However, before finding the "observed radiance", which is only affected by the low cloud, we need to remove the cirrus cloud effect from the actual observed radiance. After the cirrus cloud top height, cloud thickness, and cloud properties at the 11 μm window channel have been obtained, the reconstructed upwelling radiance $\tilde{I}_i^{\text{R}}(\infty)$ may be derived from Eq. (3.8) as follows:

$$\tilde{I}_i^R = \{ \tilde{I}_i^C(\omega) - I_2 - [1 - \tau_i^{hc}(\Delta z_h)] \tau_i(\omega, z_h) B_i[T(z_h)] \} / \tau_i^{hc}(\Delta z_h) + I_2 ,$$

$$I_2 = \int_{z_h}^{\infty} B_i[T(z)] K_i(z) dz , \quad (3.23)$$

where $\tilde{I}_i^C(\omega)$ is the satellite observed radiance. For the window channel, we may assume that the atmosphere above the cirrus cloud top is transparent, i.e., $\tau_i(\omega, z_h) \approx 1$, or $K_i(z) = 0$. So I_2 of Eq. (3.23) is approximately equal to zero, and Eq. (3.23) reduces to the form

$$\tilde{I}_i^R = \{ \tilde{I}_i^C(\omega) - [1 - \tau_i^{hc}(\Delta z_h)] \tau_i(\omega, z_h) \} / \tau_i^{hc}(\Delta z_h) . \quad (3.24)$$

After reconstructing the "observed radiance", we may then relate \tilde{I}_i^R and the low cloud top height.

To a good approximation, water clouds may be considered as blackbody radiators. Thus, the cloud transmissivity term in Eq. (3.15) may be ignored and we get

$$\tilde{I}_i^R = B_i(T_c) \tau_i(\omega, z_\ell) + \int_{z_\ell}^{\infty} B_i[T(z)] K_i(z) dz . \quad (3.25)$$

Utilizing a prescribed temperature profile and assuming that the low cloud temperature T_c is the same as the average ambient temperature, \tilde{I}_i^R is clearly a function of the low cloud top height z_ℓ . On the basis of the theoretical analysis, the relationship between \tilde{I}_i^R and z_ℓ is approximately given by the following polynomial equation:

$$z_\ell = e_0 + e_1 \tilde{I}_i^R + e_2 (\tilde{I}_i^R)^2 , \quad (3.26)$$

where the coefficients e_0 , e_1 , and e_2 are determined through empirical regression analyses. Using Eq. (3.26) the low cloud top height may be estimated from the observed radiance in the window channel.

3.3 Parameterization of Microwave Radiative Transfer in Cloudy Atmospheres

In an overcast precipitating atmosphere the cloud top height may be considered to be the cloud thickness. Moreover, the cloud reflectivity may be ignored. Thus, the upwelling brightness temperature in cloudy atmospheres at the satellite point may be decomposed into five sources as schematically illustrated in Fig. 3.3. These are (a) the direct contribution from the surface, (b) emission from the cloud layer, (c) reflection of the cloud emission from the surface, (d) the gaseous emission from the atmosphere above cloud, and (e) reflection of the gaseous emission above cloud from the surface. Thus, the brightness temperature in cloudy atmospheres may be expressed in terms of the parameterized equation in the form

$$\begin{aligned} \tilde{T}_B(\nu) = & \{ [\epsilon_V^C T_S + \epsilon_V T_C (1 - \epsilon_V)] \tau_V^C + \tau_V^C T_C \} \tau_V(\omega, z_\ell) \\ & + \int_{z_\ell}^{\infty} T(z) K_V(z) dz + (\tau_V^C)^2 (1 - \epsilon_V) \int_{z_\ell}^{\infty} \left[\frac{\tau_V(\omega, z_\ell)}{\tau_V(\omega, z)} \right]^2 T(z) K_V(z) dz, \end{aligned} \quad (3.27)$$

where ϵ_V^C denotes the cloud emissivity assuming a constant cloud temperature, ϵ_V is the surface emissivity, τ_V^C the cloud transmissivity, T_C the average cloud temperature, which is assumed to be the same as the average ambient temperature, τ_V the gaseous transmittance, z_ℓ the low cloud top height, and K_V the weighting function, which is in reference to

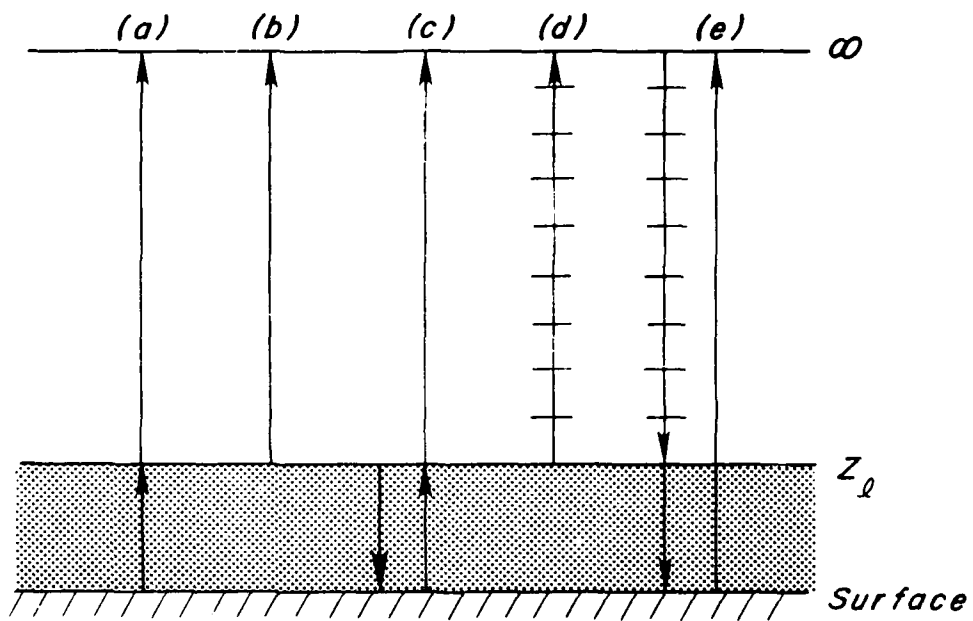


Fig. 3.3. Contributions of the upwelling brightness temperature in a cloudy atmosphere.

the top of the atmosphere.

Upon utilizing a comprehensive and rigorous microwave radiative transfer program developed at the University of Utah, the theoretically simulated data may be generated and regression equations, which express ϵ_V^C , T_V^C , and their product $\epsilon_V^C T_V^C$ as functions of the liquid water content Δw and cloud thickness Δz , maybe constructed. By means of this theoretical-empirical analysis, the following equations are obtained:

$$\epsilon_V^C = a_0 + a_1 \Delta w + a_2 \Delta w \Delta z + a_3 \Delta z + a_4 (\Delta z)^2, \quad (3.28a)$$

$$T_V^C = b_0 + b_1 \Delta w + b_2 \Delta w \Delta z + b_3 \Delta z + b_4 (\Delta z)^2, \quad (3.28b)$$

$$\epsilon_V^C T_V^C = c_0 + c_1 \Delta w + c_2 \Delta w \Delta z + c_3 \Delta z + c_4 (\Delta z)^2, \quad (3.28c)$$

Note that the above equations are linear with respect to Δw . The computed emissivity and transmissivity are highly correlated with the real values. The multiple correlation coefficient using Eq. (3.28a) and (3.28b) is equal to 0.999, while for Eq. (3.28c) it is 0.969. The latter correlation coefficient is poorer than the former because the product $\epsilon_V^C T_V^C$ increases and then decreases with increasing Δw and Δz . Since the only term containing $\epsilon_V^C T_V^C$ in Eq. (3.27) is the surface reflection of the cloud emission which contributes no more than 3% to the total upwelling brightness temperature, the error produced in the analysis using Eq. (3.28c) is insignificant.

Upon substituting Eq. (3.28) into Eq. (3.27), calculations may be carried out for the brightness temperature. Comparisons with

values obtained from our microwave radiative transfer program reveal that the accuracy of the brightness temperature computed from the parameterized equation is within about 1%. Moreover, the contribution of the last term in Eq. (3.27) for the water vapor and window channels is less than about 0.1%, and therefore it may be neglected in the numerical analysis.

Using Eqs. (3.28), emissivity and transmissivity are plotted as functions of the rainfall rate and cloud thickness for the SCAMS water vapor channel (Fig. 3.4). The similar behavior for these values can be found in the window and oxygen channels. In Fig. 3.4, it is seen that τ_V^C decreases with increasing Δw and Δz , whereas ϵ_V^C increases with increasing Δw and Δz . Their product (see Fig. 3.5) also increases with increasing Δw and Δz , implying that ϵ_V^C is a dominant factor when the product of the rainfall rate (RFR) and thickness Δz is less than 30. When the product of RFR and Δz is larger than 30, $\tau_V^C \epsilon_V^C$ begins to decrease with increasing Δw and Δz . This implies that τ_V^C is now a dominant factor. If the product of RFR and Δz , that is the cloud opacity, becomes infinite, clearly then the product of τ_V^C and ϵ_V^C equals zero. It should be noted that rainfall rate in mm/hr can be converted to liquid water content in g/m^3 through the Marshall-Palmer size distribution. The relation between rainfall rate and liquid water content is tabulated in Table 3.1.

3.4 Determination of Liquid Water Content from SCAMS Channels

The cloud liquid water content information is contained in Eq. (3.27) through values of ϵ_V^C and τ_V^C , which in turn are functions of

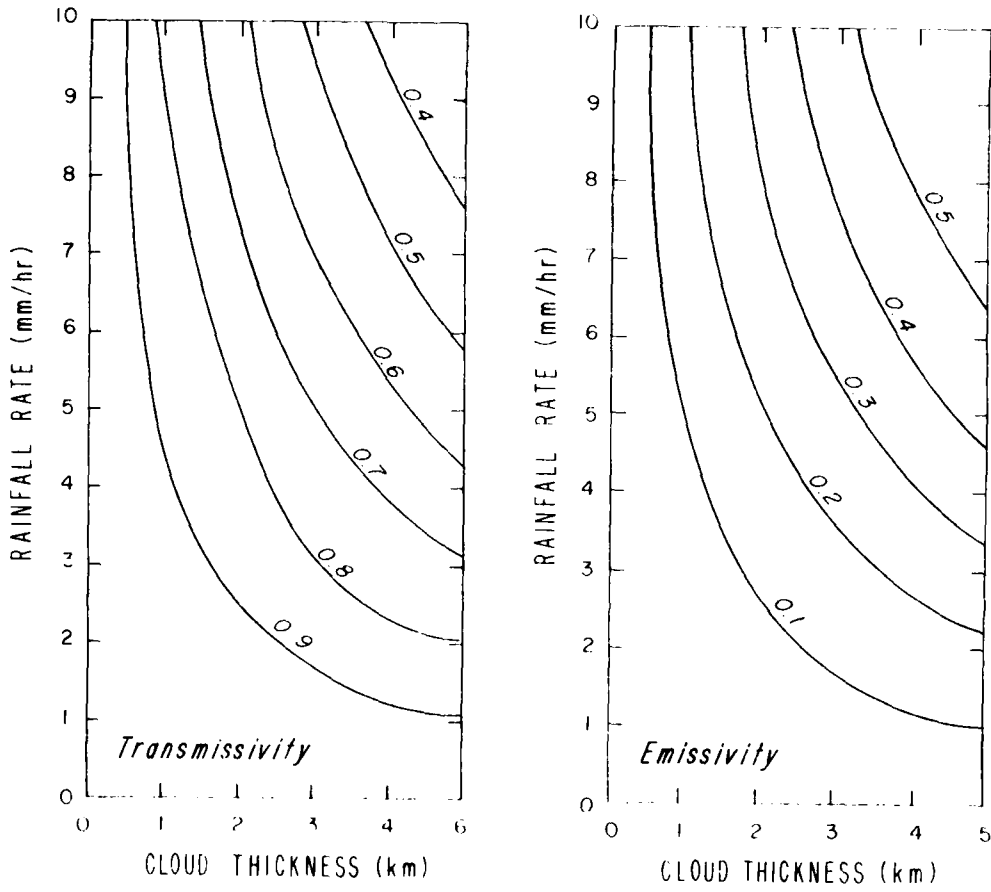


Fig. 3.4. The cloud transmissivity and emissivity as functions of the rainfall rate and cloud thickness for the SCAMS water vapor channel.

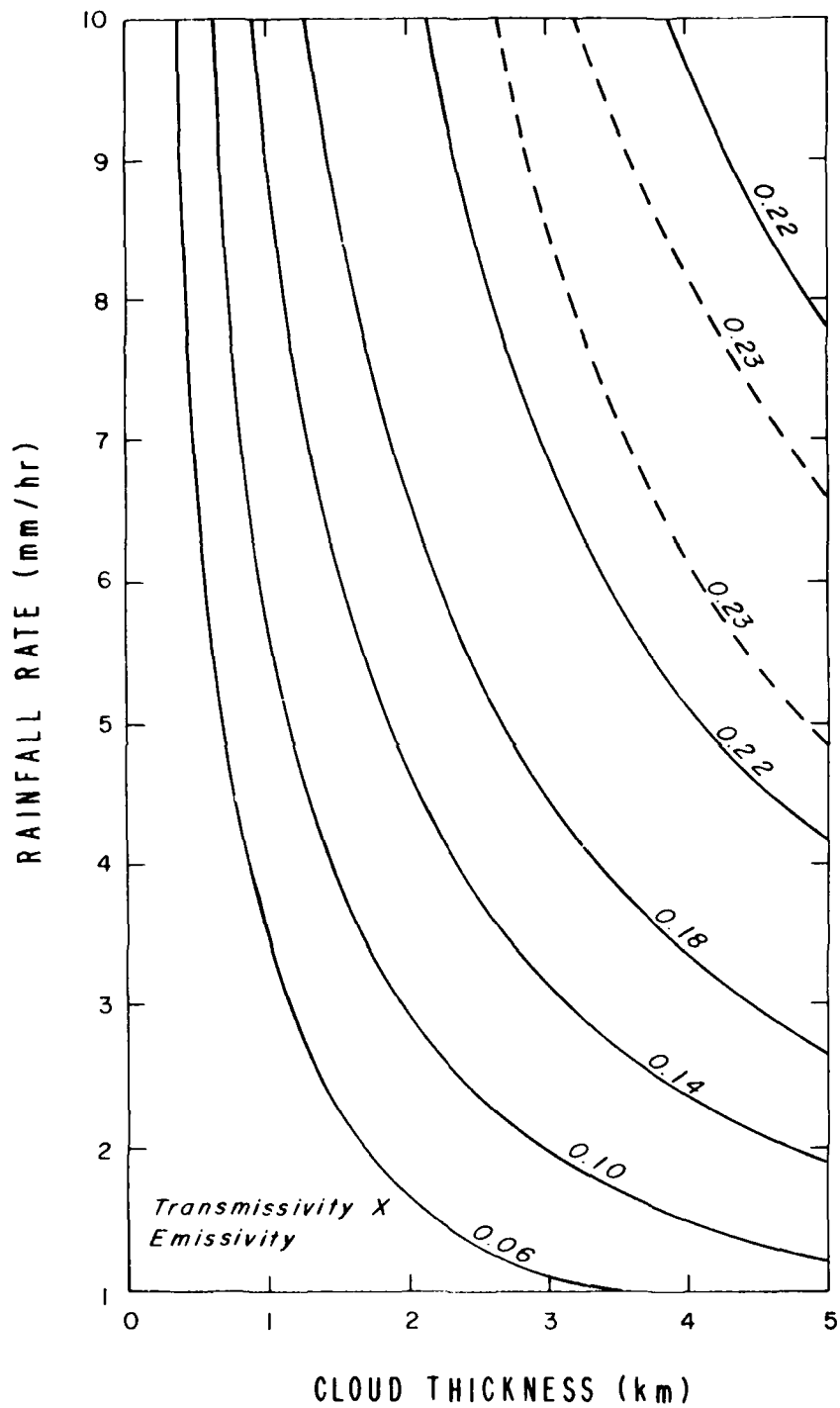


Fig. 3.5. The product of the cloud transmissivity and emissivity as a function of the rainfall rate and cloud thickness for the SCAMS water vapor channel.

Table 3.1. Relation between rainfall rate and liquid water content.

Rainfall Rate (mm/hr)	1	2	3	4	5	6	7	8	9	10
$\Delta w (\times 10^{-1})$ (g/m ³)	0.889	1.592	2.238	2.849	3.437	4.006	4.559	5.101	5.631	6.152

Δw and Δz as indicated in Eq. (3.28). Substituting Eq. (3.28) into Eq. (3.27) and after a number of mathematical manipulations, Eq. (3.27) becomes

$$T'_B(\nu) = [u_1 + u_2(z_\ell)]\Delta w + u_0 + u_3(z_\ell) + u_4(z_\ell)^2, \quad (3.29)$$

where

$$T'_B(\nu) = [\tilde{T}_B(\nu) - \int_{z_\ell}^{\infty} T(z)K_V(z)dz]/T_V(\nu, z_\ell),$$

and

$$u_i = a_i T_C + b_i T_S \epsilon_V + c_i T_C (1 - \epsilon_V), \quad i=0,1,2,3,4.$$

If the temperature and humidity profiles are prescribed, and the cloud thickness or cloud top height z_ℓ has been determined from previous analyses, then $T'_B(\nu)$ may be estimated from the observed brightness temperature $\tilde{T}_B(\nu)$. Furthermore, if we estimate ϵ_V from the SCAMS data for the water vapor and window channels utilizing an empirical equation

proposed by Waters et al. (1975), the liquid water content can then be obtained from Eq. (3.29) in the form

$$\Delta w = T_B'(v) - ([u_0 + u_3(z_\lambda) + u_4(z_\lambda)^2]) / [u_1 + u_2(z_\lambda)] . \quad (3.30)$$

We shall now describe the procedure for determining the surface emissivity from the SCAMS channels. Since the instrumental characteristics for the Nimbus 6 SCAMS channels 1 and 2 (at 22.235 and 31.650 GHz) are similar to those for the Nimbus 5 NEMS channels 1 and 2 (at 22.235 and 31.4 GHz), the equation developed by Waters et al. (1975) for calculating surface reflectivities may be used in the present numerical analysis. The surface emissivity over land can be simply estimated from the surface reflectivity R_v in the form

$$\epsilon_v = 1 - R_v . \quad (3.31)$$

According to Waters et al., the surface reflectivity for channel 2 can be approximated by

$$R_2 = \frac{[T_B(2) - T_e(2)] + [T_e(2) - T_s] \exp(-\tau_2^0)}{T_e(2)[1 - \exp(-\tau_2^0)] - T_s \exp(-\tau_2^0)} , \quad (3.32)$$

where $T_B(2)$ is the measured brightness temperature for channel 2. $T_e(2)$ is an equivalent atmospheric emission temperature for channel 2, which is approximately given by

$$T_e(2) = 0.965 \times T(850 \text{ mb}) , \quad (3.33)$$

where $T(850 \text{ mb})$ is the prescribed atmospheric temperature at the 850 mb pressure level. The atmospheric transmissivity for channel 2, $\exp(-\tau_2^0)$, is determined from the empirical equation

$$\exp(-\tau_2^0) = b \left[1 - a \left[r \frac{T_S - T_B(1)}{T_S - T_B(2)} \right]^{1/2} \right]^{-1}, \quad (3.34)$$

where $a=0.32$, $b=0.66$, and $r=R_2/R_1$, which has a value of 0.94 and 1.0 for flat water surface and land, respectively, and $T_B(1)$ is the measured brightness temperature for channel 1. By virtue of Eqs. (3.32) - (3.34), the surface reflectivity for channel 2 can be computed and the surface emissivity thus obtained from Eq. (3.31).

3.5 Results of Theoretical Analyses

In order to test the validity of the theoretical analyses outlined previously, a hypothetical atmosphere containing two-layered clouds is constructed. The cirrus cloud top is assumed to be located at 300 mb (9.358 km) for the mid-latitude summer profile with a thickness of 1 km. The low cloud top height is placed at 780 mb having a total liquid water content of 0.07 g/cm^2 . The "observed" infrared upwelling radiances for HIRS channels are computed from Eq. (3.14), while the "observed" microwave upwelling brightness temperatures for SCAMS channels are calculated from Eq. (3.27). Upon imposing different percentages of random errors on the "observed" values, computations of the cloud parameters are subsequently carried out. Results of the sequential calculations for the cirrus cloud top height, cloud thickness, low cloud top height, and cloud liquid water content are shown in Figs. 3.6. For the random error ranging from 0 to 3%, the range of the cirrus top height is

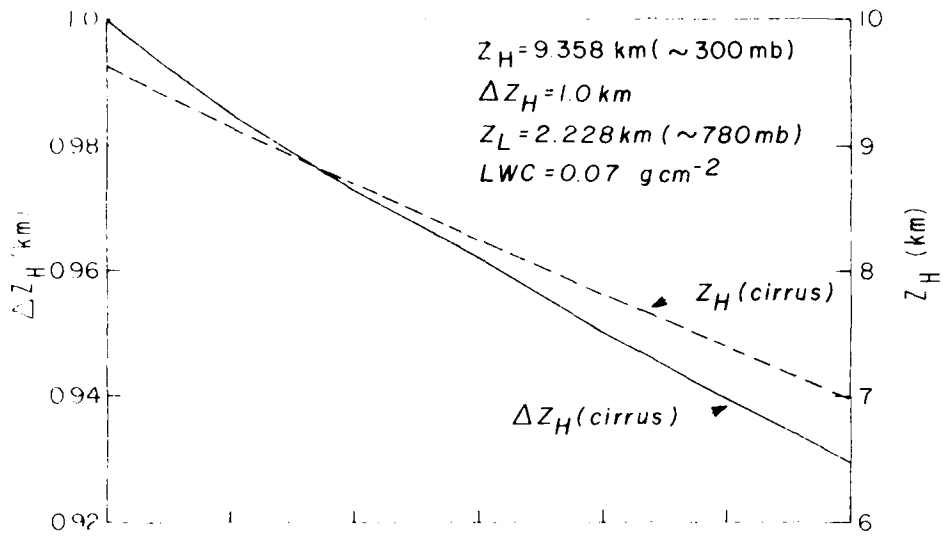


Fig. 3.6a. Hypothetical error analysis for the determination of the cirrus top height, and cloud thickness.

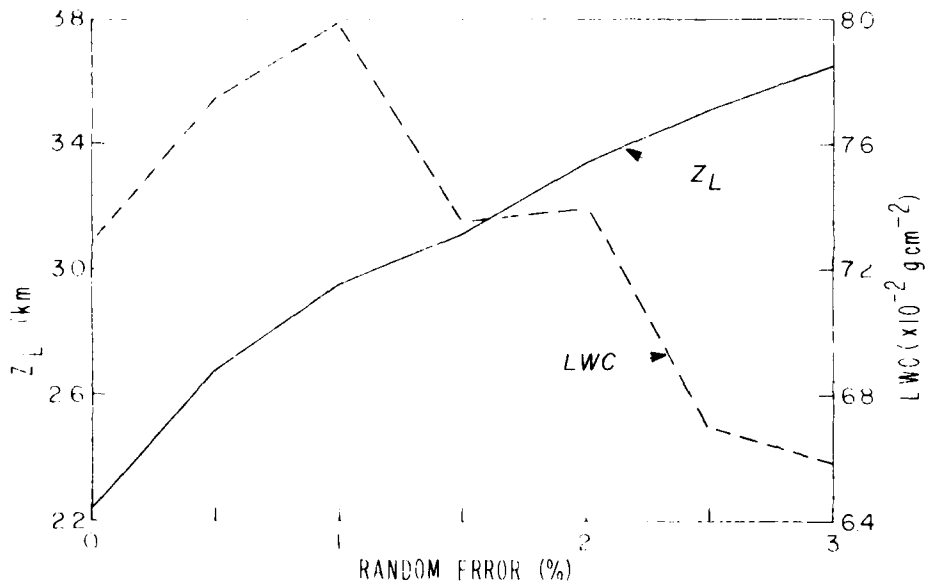


Fig. 3.6b. Same as Fig. 3.6a, except for low cloud top height and cloud liquid water content.

from 9.6 to 7.0 km. The computed height errors increase linearly with increasing random error as shown in Fig. 3.6a. Note that without imposing random errors on the "observed" values, the computed cirrus top height with a value of 9.6 km is slightly higher than the assumed value. This is due to interference from low clouds on channels 4 and 5 of the HIRS, which are used to estimate the cirrus top height. But this slight difference is not significant enough to cause errors on the sequential calculations in the numerical experiment. The increase of the computed errors for the cirrus thickness is also linear with respect to the increase of the imposed random error. However, the error range of the thickness is limited to within about 0.07 km with an assumed thickness of 1 km. The low cloud top height is calculated after the cirrus cloud effect has been removed from the HIRS window channel measurement. As shown in Fig. 3.6b, the low cloud top height increases when the cirrus top height and thickness decrease due to the increased random error. This may result from compensating effects in which the cirrus parameters are underestimated while an overestimation of the low cloud thickness produces the same upwelling radiance. The dashed line in the figure shows the computed liquid water content. The fluctuation of the liquid water content reveals a nonlinear dependence of the liquid water content on other parameters. As can be seen, even without inserting random errors, the computed liquid water content (0.073 g/cm^2) differs from the assumed value of 0.07 g/cm^2 . However, when random errors are inserted the computed liquid water content remains in the range of 0.08 to 0.066

This range appears to be acceptable in view of the difficulty involved in deriving the liquid water content from any remote

sensing and in-situ technique.

3.6 Applications to Nimbus VI HIRS and SCAMS Data

In this section, we describe the resulting cloud parameters inferred from Nimbus VI HIRS and SCAMS data for two different weather systems documented in a previous scientific report by Astling and Liou (1979). These weather systems were associated with summertime convection and wintertime mid-latitude cyclones which occurred in the United States during August 25, 1979 and February 20, 1976, respectively. On August 25, only seven cases met the criteria that infrared and microwave data from the Nimbus VI satellite are available along with conventional meteorological observations. On February 20, 1976, six cases were selected.

The cloud thickness and liquid water content derived from HIRS and SCAMS data for the August 25 cases are listed in Table 3.2. On this date, the major surface weather features, the 500 mb flow patterns, the GOES visible and infrared imagery, the radar summaries, and the precipitation amounts for six hour periods were comprehensively described in the report by Astling and Liou.

Surface reports indicated the rainfall rate at Lake Charles, Louisiana, was about 1 mm/hr at 1800 Z. The computed liquid water content, high cloud thickness, and low cloud thickness using satellite data at 1717 Z is 0.135 g cm^{-2} , 0.006 km and 3.77 km, respectively. The computed liquid water content, when converted to the rainfall rate utilizing the Marshall-Palmer size distribution, is equivalent to 5 mm/hr, which is much larger than the rainfall rate observed at the surface. Since surface, radar, and synoptic reports indicate strong

Table 3.2. Cloud thickness and liquid water content derived from Nimbus 6 HIRS and SCAMS channels.

STATION	TIME (GMT)	SURFACE REPORT	CLOUD THICKNESS (km)		LWC (g cm ⁻²)
			low	high	
Lake Charles, LA	17:17 Aug. 25	Precip. (1 mm/hr) C _b (9/10)	3.77	0.006	0.135
Peoria, IL	17:19 Aug. 25	Precip. (0.5 mm/hr) Low Cloud (10/10)	4.07	0.271	0.060
Internat'l Falls, MN	17:22 Aug. 25	Precip. (trace) Low Cloud/Cirrus (10/10)	6.48	0.194	0.005
Topeka, KS	17:19 Aug. 25	Low Cloud/Cirrus (10/10)	3.42	0.102	0.013
Green Bay, WI	17:20 Aug. 25	Total Overcast (10/10)	4.13	0.336	0.056
Dayton, OH	17:18 Aug. 25	Low Cloud (10/10)	3.437	0.043	0.037
Huntington, WV	17:18 Aug. 25	Low Cloud (10/10)	3.18	0.055	0.016

convective activity in the area the observed cumulonimbus clouds could have contained larger cloud droplets. Thus, it appears that the larger liquid water content derived from the microwave channels may well represent the actual moisture present within the cumulonimbus.

We found a liquid water content value of 0.005 g cm^{-2} for the International Falls case. Our computed value matches quite well with the surface precipitation report. Although the low cloud thickness is estimated to be about 6.5 km, the cloud might well contain a large number of ice crystals and small water droplets. Under this condition only large raindrops near the cloud bottom would contribute significantly to the signature in the microwave region.

At 1719 Z 25 August, according to an 1800 Z surface report and 1900 Z GOES infrared imagery, Topeka, Kansas was covered by a low cloud deck with thin cirrus aloft. Inspection of the sequential surface maps reveals a major cold front passed Topeka at about 1200 Z. As described in the report by Astling and Liou, clouds in the post frontal region tend to be less convective and contain smaller amounts of moisture. Thus, the computed cloud liquid water content of 0.013 g cm^{-2} (equivalent to 0.4 mm/hr rainfall rate) with 3.42 and 0.1 km for low and high cloud thickness, respectively, appears to agree well with synoptic observations.

The precipitation report from Peoria, Illinois at 1800 Z was 0.5 mm/hr rainfall rate. The calculated liquid water content is 0.06 g cm^{-2} , which is equivalent to less than 1 mm/hr rainfall rate. Again, the larger computed value for the cloud liquid water content may be associated with a well-developed convective cloud.

The strong frontal activity did not produce precipitation at Green Bay, Wisconsin or Dayton, Ohio. However, it is believed that a large amount of moisture was present in the atmosphere in the Great Lakes area. The computed cloud liquid water content for the Green Bay case is 0.056 g cm^{-2} , which would produce 1.7 mm/hr rainfall rate if the total cloud moisture were converted to precipitation. The cloud liquid water content for the Dayton case is 0.037 g cm^{-2} , equivalent to 1.3 mm/hr rainfall rate.

The overcast low cloud reported at Huntington, West Virginia, did not contain as much moisture as the Great Lakes cases. The calculated values show the cloud liquid water content at Huntington was about 0.016 g cm^{-2} , which is approximately equal to a 0.5 mm/hr rainfall rate. The small cloud liquid water content obtained for this case might be due to the lack of a moisture supply, since the station was far east of the very active frontal zone.

The cloud thickness and liquid water content derived from HIRS and SCAMS data for the February 20 and 21 cases are listed in Table 3.3. In reference to the synoptic analyses described by Astling and Liou, the major trough with low center located in Kansas brought abundant amount of moisture from the Gulf of Mexico to Louisiana and into Arkansas through the warm front. The surface report of Little Rock, Arkansas at 1800 Z 20 February, indicated a total obstruction due to low cloud. The computed results revealed that the cloud development at Little Rock was quite stable since the low cloud thickness only extended to about 1.46 km. The total cloud liquid water content was estimated to be about 0.0067 g cm^{-2} , which is equivalent to about

Table 3.3 Cloud thickness and liquid water content derived from Nimbus VI HIRS and SCAMS channels for February 20 and 21 cases.

STATION	TIME (GMT)	SURFACE REPORT	CLOUD THICKNESS (km)		LWC (g cm ⁻²)
			low	high	
Little Rock, ARK	17:11 Feb. 20	Low cloud (10/10)	1.46	0.05	0.0067
Rapid City, S.D.	17:14 Feb. 20	Low cloud (10/10)	3.23	0.47	0.01
Spokane WA.	10:02 Feb. 20	Low cloud (10/10) with fog	5.09	0.03	0.22
Huntington, W. VA.	16:30 Feb. 21	Low cloud (10/10)	1.17	0.92	0.078
Dayton, OH	16:30 Feb. 21	Precipitation (2 mm/hr) Low cloud (10/10)	3.85	0.39	0.30
Peoria, IL.	16:31 Feb. 21	Precipitation (0.5 mm/hr) Low cloud	3.88	0.52	0.40

0.7 mm/hr rainfall rate.

At the same time, a moist tongue at 850 mb stretched from Gulf coast along eastern Texas and Louisiana, across Arkansas, Iowa, into southern South Dakota. Rapid City, South Dakota, reported an overcast low fractostratus and/or fractocumulus condition with a ceiling near 1,000 ft. according to the 1800 Z surface report. These cloud types are associated with the approaching cold front. The results we obtained showed that Rapid City was covered by a low cloud deck having a 3.2 km thickness and a thin cirrus cloud with a 0.47 km thickness. The cloud liquid water content was found to be about 0.01 g cm^{-2} , which is equivalent to about 0.35 mm/hr rainfall rate.

In addition to the low pressure centered in Kansas, another low pressure was located just off the northeast Pacific Ocean. This system moved southeastward into the state of Washington. The strong pressure gradients and cyclonically curved isobars brought a significant amount of Pacific moisture ashore. The surface weather observation at Spokane, Washington at 1800 Z 20 February reported a low cloud total obstruction with cloud ceiling height at about 300 ft. Ground fog and near zero visibility were also reported. The computed results indicated that a low cloud with a thickness of 5.09 km and liquid water content of 0.22 g cm^{-2} was present at Spokane under the satellite pass at 1902 Z.

The precipitation activity was most intense along the occluded and cold fronts located in the midwest during the 12 hours prior to 0000 Z 22 February. Six hour rainfall amounts were found to be in excess of 1 inch at several stations along the cold front.

At Dayton, Ohio, a 2 mm/hr rainfall rate and a low cloud ceiling near 400 ft. were reported at 1800 Z 21 February. The computed results show that there were thick low clouds having total liquid water content of as much as 0.3 g cm^{-2} (equivalent to about 10 mm/hr rainfall rate). The results appear to be in qualitative agreement with the surface and synoptic reports which indicated strong ascending motions at Dayton.

The retrieved results for Peoria, Illinois show a low cloud deck 3.88 km thick with a large liquid water content of 0.4 g cm^{-2} (~11 mm/hr rainfall rate). This value is much larger than the observed rainfall rate of 0.5 mm/hr. However, according to the index of stability from the synoptic data, the area showed strong ascending motions which could produce large water droplets within the cloud, and hence, large liquid water content.

The retrieved cloud parameters for the Huntington, Virginia case reveal that the low and high cloud thicknesses are 1.17 and 0.92 km, respectively, and the liquid water content is 0.078 g cm^{-2} . The reason for the small liquid water content is probably due to the relatively stable atmosphere surrounding the area. The radiosonde observations indicated that the relative humidity was 90% at 300 mb but was less than 50% at 850 mb.

In summary, we have applied the cloud sounding technique developed from the parameterization of infrared and microwave radiative transfer to the Nimbus VI HIRS and SCAMS data. The satellite retrieved cloud parameters from selected infrared and microwave channels appear to be in qualitative agreement with the available synoptic, radiosonde,

surface and radar reports. The results illustrated in this section are indeed encouraging. Thus, it appears that applications of the cloud sounding technique developed in this report for the mapping of three-dimensional cloud compositions and structure over the globe, utilizing the available satellite infrared and microwave data, may be carried out.

SECTION 4

CONCLUSIONS

In this report, we have presented two areas of the research results concerning the sounding of cloud parameters from orbiting meteorological satellites. First, in conjunction with the cloud sounding utilizing the Nimbus 6 ESMR channel, we have developed a microwave radiative transfer program in which the polarization effect is included so that the vertically and horizontally polarized brightness temperatures can be computed and compared with observed data. The program involves the use of the discrete-ordinate method in solving the fundamental transfer equation governing absorbing molecules and Rayleigh particulates in the microwave region. Analytical solutions, assuming an isothermal cloud temperature, are derived for both vertical and horizontal polarization components in which the polarization characteristics of the surface emissivity is taken into account.

Comparisons between the theoretically computed brightness temperature, employing the available temperature and mixing ratio profiles from radiosonde, and the observed data are carried out for selected clear, cloudy, and precipitating atmospheres over unpolarized land and polarized ocean surfaces. Fairly good agreement is found between the computed results and observed data with differences within about 6°K. It may be concluded therefore that the radiative transfer program developed in this study appears to be quite reliable despite the difficulty involved in the determination of the surface emissivity in all weather conditions. The microwave radiative transfer program is then used to perform theoretical

sensitivity analyses to investigate the effects of the emergent angle, rainfall rate, cloud thickness, and atmospheric profile on the brightness temperatures for vertical and horizontal polarization components. Subsequently, we develop a simple empirical-theoretical approach to recover the cloud liquid water content and cloud thickness from vertical and horizontal brightness temperatures. Using the available ESMR data over ocean areas, we illustrate that reasonable cloud liquid water contents and cloud thicknesses may be derived from a set of linear equations. However, owing to the unavailability of surface weather observations over ocean, we have been unable to verify the degree of reliability for these retrieval analyses.

It should be pointed out here that the ESMR program utilizes highly simplified linear equations in the retrieval of cloud parameters. The next hierarchy of the theoretical-empirical approach would be the development of high order equations for retrieval purposes on the basis of the physical and mathematical analyses of the solution of the microwave radiative transfer equation. Moreover, one additional improvement to the theoretical microwave radiative transfer program would be to remove the Rayleigh approximation in the treatment of the source function. It is believed that the analysis involving the Nimbus 6 ESMR data illustrated in this report may be of direct use to the DMSP SSM/I multispectral microwave imager to be flown in 1983 for applications and operational uses.

The second area of research results presented in this report is concerned with the exploitation of cloud sounding techniques utilizing a combination of infrared and microwave channels. In connection with this purpose, we have first developed parameterized equations for infrared and microwave radiation transfer in atmospheres containing multi-layered clouds.

Parameterizations of the infrared and microwave radiation transfer makes use of the physical and geometrical principles, and they are verified through rigorous transfer programs developed at the University of Utah in the last few years. The parameterized equations are then employed to retrieve high cloud top height, high cloud thickness, low cloud top height, and cloud liquid water content successively utilizing selected HIRS and SCAMS channels.

Hypothetical error analyses have been performed and we find that the retrieval technique involving the use of both infrared and microwave channels appears to be theoretically rigorous and practically workable. Consequently, we have applied this cloud sounding technique to the Nimbus 6 HIRS and SCAMS data for a number of carefully selected cases associated with summertime convective cloud systems and wintertime large scale synoptic cyclones described in the report by Astling and Liou (1979). High and low cloud thicknesses and total liquid water content are recovered from a combination of selected HIRS and SCAMS channels and are compared with the available synoptic, radiosonde, surface, and radar observations and satellite photographs. Qualitative agreement is found between the retrieved cloud parameters and the results estimated from synoptic data and analyses.

The development of the cloud sounding technique using combined infrared and microwave channels is quite significant in view of the relative advantages and shortcomings of the infrared and microwave frequencies with respect to cloud sounding problem. It may be pertinent to point out here that microwave frequencies penetrate through low clouds, which are opaque in the infrared region, and that high clouds normally affect significantly the transfer of infrared radiation but have little effect on the microwave propagation. It is quite clear therefore that a combination

of infrared and microwave frequencies is vitally essential to the determination of the vertical cloud structure and compositions. In this investigation, we have demonstrated convincingly the possibility of deriving the vertical cloud parameters based on a number of carefully selected cases. Thus, further investigations and verifications may pave the way for the mapping of three-dimensional cloud parameters over the global space. Finally, it should be pointed out that the fundamental difficulty in the development of the cloud sounding technique from orbiting meteorological satellites has been the lack of cloud physics data for intercomparisons and verifications. In this connection, it appears logical to suggest that a carefully designed field experiment involving the simultaneous satellite radiation program, aircraft cloud physics program, and synoptic and radiosonde observations be carried out when the developed cloud sounding technique using both infrared and microwave sounders appears promising. The accurate and reliable cloud sounding program in an operational mode certainly will enhance and improve the ongoing AFGWC 3D NEPH program. Moreover, it also is vitally important to the understanding of the radiative budget and climate of the earth-atmosphere system.

REFERENCES

- Astling, E. G. and K. N. Liou, 1979: Analyze, calculate and develop techniques for weathersatellite imagery data. Final report, Air Force Geophysics Laboratory, AFGL-TR-79-0140.
- Chandrasekhar, S., 1950: Radiative Transfer. Dover, 393 pp.
- Feddes, R. G. and K. N. Liou, 1978: Atmospheric ice and water content derived from parameterization of Nimbus 6 High Resolution Infrared Sounder data. *J. Appl. Meteor.*, 17, 536-551.
- Hall, J., 1979: A dynamic and synoptic study of a wintertime cyclone using geostationary and polar orbiting satellite data. Master's thesis, Department of Meteorology, University of Utah, Salt Lake City, Utah.
- Hollinger, J. R., 1973: Microwave properties of a calm sea. Naval Research Laboratory Rep. 7110-2, Washington, D. C., 69 pp.
- Hunt, G. E., 1973: Radiative properties of terrestrial clouds at visible and infrared thermal window wavelengths. *Quart. J. R. Met. Soc.*, 99, 346-369.
- Liou, K. N., T. L. Stoffel, R. G. Feddes and J. T. Bunting, 1978: Radiative properties of cirrus clouds in NOAA 4 VTPR channels: Some explorations of cloud scenes from satellites. *Pure and Appl. Geophy.*, 116, No. 6, 1007-1029.
- Liou, K. N. and A. D. Duff, 1979: Atmospheric liquid water content derived from parameterization of Nimbus 6 Scanning Microwave Spectrometer data. *J. Appl. Meteor.*, 18, 99-103.
- McCleese, D. J. and I. S. Wilson, 1976: Cloud top heights from temperature sounder instruments. *Quart. J. R. Met. Soc.*, 102, 781-790.

AD-A097 592

UTAH UNIV SALT LAKE CITY DEPT OF METEOROLOGY F/G 4/2
DEVELOPMENT OF INFRARED AND MICROWAVE TECHNIQUES FOR CLOUD PARA--ETC(U)
AUG 80 K LIOU, H Y YEH, F M CHEN, K HUTCHISON F19628-78-C-0130

AFGL-TR-80-0263

NL

UNCLASSIFIED

FORM 1
1-78



END
DATE
FILMED
9-81
DTIC

Staff Members, 1975: The Nimbus VI User's Guide. Goddard Space Flight Center, Greenbelt, Maryland, 227 pp.

Waters, J. W., et al., 1975: Remote sensing of atmospheric temperature profiles with Nimbus 5 Microwave Spectrometer. J. Atmos. Sci., 32, 1953-1969.

Printed by
United States Air Force
Hanscom AFB, Mass. 01731

